

sangkuriang: A pseudo-spectral Python library for Korteweg-de Vries soliton simulation

Sandy H. S. Herho^{1,2,3,*}, Faruq Khadami⁴, Iwan P. Anwar⁴, and Dasapta E. Irawan⁵

¹Department of Earth and Planetary Sciences, University of California, Riverside, CA 92521, USA

²Ronin Institute for Independent Scholarship 2.0, Sacramento, CA 95816, USA

³School of Systems Science and Industrial Engineering, State University of New York, Binghamton, NY 13902, USA

⁴Applied and Environmental Oceanography Research Group, Bandung Institute of Technology, Bandung 40132, Indonesia

⁵Applied Geology Research Group, Bandung Institute of Technology, Bandung 40132, Indonesia

*e-mail: sandy.herho@email.ucr.edu

Abstract

The Korteweg-de Vries (KdV) equation serves as a foundational model in nonlinear wave physics, describing the balance between dispersive spreading and nonlinear steepening that gives rise to solitons. This article introduces `sangkuriang`, an open-source Python library for solving this equation using Fourier pseudo-spectral spatial discretization coupled with adaptive high-order time integration. The implementation leverages just-in-time (JIT) compilation for computational efficiency while maintaining accessibility for instructional purposes. Validation encompasses progressively complex scenarios including isolated soliton propagation, symmetric two-wave configurations, overtaking collisions between waves of differing amplitudes, and three-body interactions. Conservation of the classical invariants is monitored throughout, with deviations remaining small across all test cases. Measured soliton velocities conform closely to theoretical predictions based on the amplitude-velocity relationship characteristic of integrable systems. Complementary diagnostics drawn from information theory and recurrence analysis confirm that computed solutions preserve the regular phase-space structure expected for completely integrable dynamics. The solver outputs data in standard scientific formats compatible with common analysis tools and generates visualizations of spatiotemporal wave evolution. By combining numerical accuracy with practical accessibility on modest computational resources, `sangkuriang` offers a platform suitable for both classroom demonstrations of nonlinear wave phenomena and exploratory research into soliton dynamics.

Keywords: adaptive time integration, Korteweg–de Vries equation, pseudo-spectral methods, soliton dynamics

1 Introduction

The Korteweg–de Vries (KdV) equation occupies a distinguished position in the undergraduate and graduate physics curriculum, serving as the canonical example of a nonlinear partial differential equation (PDE) that admits exact analytical solutions with remarkable physical properties [3]. First derived in the context of shallow water waves [1], this equation demonstrates how the competing effects of nonlinearity and dispersion can achieve a delicate balance, producing localized wave structures—solitons—that propagate without change of form and survive mutual collisions intact [2]. The discovery that such behavior arises from complete integrability, with an infinite hierarchy of conservation laws accessible through inverse scattering techniques [4, 5], has made the KdV equation a cornerstone for teaching nonlinear dynamics, Hamiltonian systems, and mathematical physics at the advanced undergraduate and graduate levels [6].

Despite the rich analytical structure of soliton theory, students often struggle to develop physical intuition for nonlinear wave phenomena from analytical treatments alone. The interplay between steepening and dispersion, the amplitude-dependent velocity of solitons, and the elastic nature of their collisions are concepts that benefit enormously from direct visualization and numerical experimentation [7]. Computational laboratories, in which students can modify initial conditions, vary physical parameters, and observe the resulting dynamics, offer pedagogical opportunities that complement traditional analytical instruction [8]. Such exercises allow learners to discover the defining characteristics of solitons empirically—for instance, that taller waves travel faster, or that collisions produce phase shifts but preserve wave identities—before or alongside formal derivations.

The choice of programming environment significantly influences the accessibility and effectiveness of computational physics education. Python has emerged as the dominant language for scientific computing instruction, owing to its readable syntax, extensive ecosystem of numerical libraries, and low barrier to entry for students without prior programming experience [9, 10]. The availability of high-quality implementations of fundamental algorithms—fast Fourier transforms (FFT), adaptive differential equation solvers, and array operations—within freely distributed libraries such as NumPy and SciPy [11, 12] enables students to focus on physical concepts rather than low-level implementation details. Furthermore, recent developments in just-in-time (JIT) compilation through libraries such as Numba [13] permit Python codes to achieve performance competitive with compiled languages, removing the traditional trade-off between ease of development and computational speed [14]. These

characteristics have established Python as the preferred platform for computational physics courses at institutions worldwide [15, 16].

Pseudo-spectral methods represent a particularly instructive approach to the numerical solution of PDEs, combining the elegance of Fourier analysis with practical computational efficiency [17, 18]. By representing spatial derivatives as multiplications in wavenumber space, these methods achieve high accuracy for smooth periodic solutions while introducing students to concepts—the discrete Fourier transform (DFT), aliasing, spectral convergence—that recur throughout computational physics and signal processing [19, 20]. The KdV equation, with its combination of nonlinear and dispersive terms operating on smooth soliton profiles, provides an ideal context for introducing pseudo-spectral techniques at the graduate level.

This article presents `sangkuriang`, an open-source Python library for solving the KdV equation, designed with both pedagogical clarity and computational efficiency as objectives. The implementation employs Fourier pseudo-spectral spatial discretization coupled with adaptive eighth-order Runge–Kutta time integration via the Dormand–Prince 8(5,3) (DOP853) method [21, 22]. Performance-critical routines are accelerated through Numba JIT compilation with support for multi-core parallelization, enabling research-grade simulations on modest hardware. The library provides a command-line interface for immediate use with predefined test cases, a Python Application Programming Interface (API) for programmatic access, and outputs simulation data in Network Common Data Format (NetCDF) format following Climate and Forecast (CF) conventions [23] for compatibility with standard analysis tools. Beyond basic simulation capabilities, the solver incorporates diagnostic routines for monitoring conservation laws and generating animated visualizations, enabling students to verify numerical accuracy and explore the mathematical structure of integrable systems. The software is freely available from the Python Package Index (PyPI) and distributed under a permissive open-source license.

2 Methods

2.1 Model Description

The KdV equation constitutes one of the most fundamental nonlinear PDEs in mathematical physics, governing the propagation of weakly nonlinear, weakly dispersive waves in various physical contexts [1, 2]. We derive this equation from first principles beginning with the three-dimensional Navier–Stokes equations, following the established asymptotic analysis framework [7, 6].

Consider an inviscid, incompressible fluid occupying a domain bounded below by a rigid horizontal bottom at $z = 0$ and above by a free surface at $z = h_0 + \eta(x, y, t)$, where h_0 denotes the undisturbed depth and η represents the free surface displacement (Figure 1). The fluid is subject to gravitational acceleration g acting in the negative z -direction.

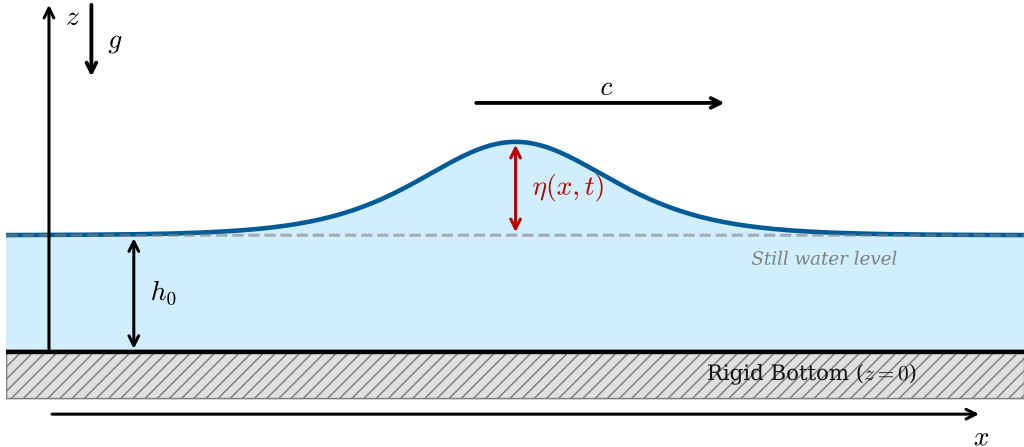


Figure 1: Schematic of the shallow water wave domain. The fluid occupies a region bounded below by a rigid horizontal bottom at $z = 0$ and above by a free surface at $z = h_0 + \eta(x, t)$, where h_0 denotes the undisturbed water depth and $\eta(x, t)$ represents the free surface displacement. Gravitational acceleration g acts in the negative z -direction, and wave propagation occurs along the x -axis with phase speed c .

For an inviscid fluid, the three-dimensional incompressible Euler equations governing the velocity field $\mathbf{u} = (u, v, w)$ and pressure p read

$$\nabla \cdot \mathbf{u} = \frac{\partial u}{\partial x} + \frac{\partial v}{\partial y} + \frac{\partial w}{\partial z} = 0, \quad (1)$$

$$\frac{\partial u}{\partial t} + u \frac{\partial u}{\partial x} + v \frac{\partial u}{\partial y} + w \frac{\partial u}{\partial z} = -\frac{1}{\rho} \frac{\partial p}{\partial x}, \quad (2)$$

$$\frac{\partial v}{\partial t} + u \frac{\partial v}{\partial x} + v \frac{\partial v}{\partial y} + w \frac{\partial v}{\partial z} = -\frac{1}{\rho} \frac{\partial p}{\partial y}, \quad (3)$$

$$\frac{\partial w}{\partial t} + u \frac{\partial w}{\partial x} + v \frac{\partial w}{\partial y} + w \frac{\partial w}{\partial z} = -\frac{1}{\rho} \frac{\partial p}{\partial z} - g, \quad (4)$$

where ρ is the constant fluid density. These equations are supplemented by boundary conditions at the bottom and free surface [24, 25].

At the rigid bottom $z = 0$, the impermeability condition requires

$$w = 0 \quad \text{at} \quad z = 0. \quad (5)$$

At the free surface $z = h_0 + \eta(x, y, t)$, the kinematic boundary condition states that fluid particles on the surface remain on the surface:

$$w = \frac{\partial \eta}{\partial t} + u \frac{\partial \eta}{\partial x} + v \frac{\partial \eta}{\partial y} \quad \text{at} \quad z = h_0 + \eta, \quad (6)$$

and the dynamic boundary condition requires continuity of normal stress, which for an inviscid fluid with negligible surface tension reduces to

$$p = p_{\text{atm}} \quad \text{at} \quad z = h_0 + \eta, \quad (7)$$

where p_{atm} is the constant atmospheric pressure.

We now restrict attention to unidirectional wave propagation along the x -axis, setting $v = 0$ and $\partial/\partial y = 0$. The governing equations (1)–(4) reduce to the two-dimensional system

$$\frac{\partial u}{\partial x} + \frac{\partial w}{\partial z} = 0, \quad (8)$$

$$\frac{\partial u}{\partial t} + u \frac{\partial u}{\partial x} + w \frac{\partial u}{\partial z} = -\frac{1}{\rho} \frac{\partial p}{\partial x}, \quad (9)$$

$$\frac{\partial w}{\partial t} + u \frac{\partial w}{\partial x} + w \frac{\partial w}{\partial z} = -\frac{1}{\rho} \frac{\partial p}{\partial z} - g. \quad (10)$$

To derive the shallow water equations, we introduce characteristic scales: λ for horizontal length, h_0 for vertical length, a for wave amplitude, λ/c_0 for time (where $c_0 = \sqrt{gh_0}$ is the linear long-wave speed), c_0 for horizontal velocity, and ρgh_0 for pressure. The dimensionless variables are defined as

$$\tilde{x} = \frac{x}{\lambda}, \quad \tilde{z} = \frac{z}{h_0}, \quad \tilde{t} = \frac{c_0 t}{\lambda}, \quad \tilde{\eta} = \frac{\eta}{a}, \quad \tilde{u} = \frac{u}{c_0}, \quad \tilde{w} = \frac{w\lambda}{c_0 h_0}, \quad \tilde{p} = \frac{p - p_{\text{atm}}}{\rho g h_0}. \quad (11)$$

Two fundamental small parameters emerge naturally: the amplitude parameter $\alpha = a/h_0 \ll 1$ measuring wave nonlinearity, and the dispersion parameter $\beta = (h_0/\lambda)^2 \ll 1$ quantifying the shallowness of the water [26].

Substituting the scalings (11) into equations (8)–(10) and dropping tildes for clarity, we obtain the dimensionless system

$$\frac{\partial u}{\partial x} + \frac{\partial w}{\partial z} = 0, \quad (12)$$

$$\frac{\partial u}{\partial t} + \alpha \left(u \frac{\partial u}{\partial x} + w \frac{\partial u}{\partial z} \right) = -\frac{\partial p}{\partial x}, \quad (13)$$

$$\beta \left[\frac{\partial w}{\partial t} + \alpha \left(u \frac{\partial w}{\partial x} + w \frac{\partial w}{\partial z} \right) \right] = -\frac{\partial p}{\partial z} - 1. \quad (14)$$

The factor β multiplying the left-hand side of equation (14) indicates that vertical accelerations are negligible in the shallow water limit $\beta \rightarrow 0$ [27].

In the leading-order shallow water approximation ($\beta = 0$), equation (14) reduces to the hydrostatic balance

$$\frac{\partial p}{\partial z} = -1, \quad (15)$$

which, upon integration from z to the free surface $z = 1 + \alpha\eta$ using the dynamic boundary condition $p = 0$ at $z = 1 + \alpha\eta$, yields

$$p = 1 + \alpha\eta - z. \quad (16)$$

Thus, the horizontal pressure gradient becomes

$$\frac{\partial p}{\partial x} = \alpha \frac{\partial \eta}{\partial x}, \quad (17)$$

independent of z , implying that the horizontal velocity u is also independent of depth at leading order.

Integrating the continuity equation (12) from $z = 0$ to $z = 1 + \alpha\eta$ and applying the boundary conditions (5) and (6), we obtain

$$\frac{\partial \eta}{\partial t} + \frac{\partial}{\partial x} [(1 + \alpha\eta)u] = 0. \quad (18)$$

Combining with the horizontal momentum equation (13) and pressure gradient (17), we arrive at the nonlinear

shallow water equations in dimensionless form [24]

$$\frac{\partial \eta}{\partial t} + \frac{\partial}{\partial x} [(1 + \alpha\eta)u] = 0, \quad (19)$$

$$\frac{\partial u}{\partial t} + \alpha u \frac{\partial u}{\partial x} + \frac{\partial \eta}{\partial x} = 0. \quad (20)$$

These equations are exact within the hydrostatic shallow water approximation but remain coupled and nonlinear.

To incorporate weak dispersion and derive the KdV equation, we retain terms of order β in the vertical momentum equation (14). The regime $\alpha \sim \beta \sim \mathcal{O}(\delta) \ll 1$ with δ representing a single small parameter defines the Boussinesq scaling, wherein nonlinear and dispersive effects balance to produce solitary wave solutions [26]. Under this scaling, we seek asymptotic solutions in the form of perturbation expansions

$$\eta(\xi, \tau) = \delta\eta_1(\xi, \tau) + \delta^2\eta_2(\xi, \tau) + \mathcal{O}(\delta^3), \quad (21)$$

$$u(\xi, \tau) = \delta u_1(\xi, \tau) + \delta^2 u_2(\xi, \tau) + \mathcal{O}(\delta^3), \quad (22)$$

where $\delta = \sqrt{\alpha} = \sqrt{\beta}$ serves as the expansion parameter. Substituting expansions (21) and (22) into the shallow water equations and collecting terms of equal powers in δ , we obtain at leading order $\mathcal{O}(\delta)$ the linearized wave equations

$$\frac{\partial \eta_1}{\partial \tau} + \frac{\partial u_1}{\partial \xi} = 0, \quad (23)$$

$$\frac{\partial u_1}{\partial \tau} + \frac{\partial \eta_1}{\partial \xi} = 0. \quad (24)$$

These admit right-going wave solutions of the form $\eta_1 = f(\xi - \tau)$ and $u_1 = f(\xi - \tau)$, where f is an arbitrary waveform propagating with dimensionless speed unity (dimensional speed $c_0 = \sqrt{gh_0}$).

At the next order $\mathcal{O}(\delta^2)$, nonlinear and dispersive corrections emerge [3]:

$$\frac{\partial \eta_2}{\partial \tau} + \frac{\partial u_2}{\partial \xi} = -\frac{\partial}{\partial \xi}(\eta_1 u_1), \quad (25)$$

$$\frac{\partial u_2}{\partial \tau} + \frac{\partial \eta_2}{\partial \xi} = -u_1 \frac{\partial u_1}{\partial \xi} + \frac{1}{3} \frac{\partial^3 u_1}{\partial \xi^2 \partial \tau}. \quad (26)$$

The nonlinear term $-\partial_\xi(\eta_1 u_1)$ in equation (25) arises from the advection of mass by the wave motion, while the dispersive term $\frac{1}{3} \partial_\xi^2 \partial_\tau u_1$ in equation (26) originates from the vertical acceleration induced by the sloping bottom pressure distribution [27].

To eliminate secular growth and derive a consistent evolution equation, we introduce the stretched slow variables $X = \delta(\xi - \tau)$ and $T = \delta^2 \tau$, representing a coordinate system moving with the linear wave speed and a slow time scale appropriate for observing cumulative nonlinear and dispersive effects [6]. We seek solutions in the form $\eta_1 = U(X, T)$ and apply the multiple scales method. The chain rule yields

$$\frac{\partial}{\partial \xi} = \delta \frac{\partial}{\partial X}, \quad \frac{\partial}{\partial \tau} = -\delta \frac{\partial}{\partial X} + \delta^2 \frac{\partial}{\partial T}. \quad (27)$$

Combining the solvability conditions at order $\mathcal{O}(\delta^3)$ to suppress resonant secular terms, and transforming back to dimensional variables through the scalings $x = \lambda X$, $t = \lambda T \sqrt{h_0/g}$, and $\eta = aU$, we obtain the canonical KdV equation in dimensional form [7]

$$\frac{\partial \eta}{\partial t} + c_0 \frac{\partial \eta}{\partial x} + \frac{3c_0}{2h_0} \eta \frac{\partial \eta}{\partial x} + \frac{c_0 h_0^2}{6} \frac{\partial^3 \eta}{\partial x^3} = 0, \quad (28)$$

where $c_0 = \sqrt{gh_0}$ denotes the linear shallow water wave speed. This formulation makes explicit the physical origins of each term: the second term represents linear wave propagation, the third term captures amplitude-dependent steepening (nonlinearity), and the fourth term describes frequency-dependent dispersion.

For computational implementation and to emphasize the balance between nonlinearity and dispersion, we transform equation (28) to a traveling coordinate frame $\chi = x - c_0 t$ and define $u(\chi, t) = \eta(x, t)$. Furthermore, we introduce dimensionless parameters $\varepsilon = 3c_0/(2h_0)$ [m^{-1}] characterizing the nonlinearity strength and $\mu = c_0 h_0^2/6$ [m^3/s] quantifying dispersion. This yields the standard form employed in the numerical solver [17, 20]

$$\frac{\partial u}{\partial t} + \varepsilon u \frac{\partial u}{\partial x} + \mu \frac{\partial^3 u}{\partial x^3} = 0, \quad (29)$$

where we have relabeled $\chi \rightarrow x$ for notational simplicity. In equation (29), $u(x, t)$ represents the wave amplitude field [m], with spatial coordinate x [m] and temporal coordinate t [s]. The remarkable property of this equation lies in the exact balance between the quadratic nonlinear term $\varepsilon u \partial_x u$, which steepens wave profiles and would induce shock formation in isolation, and the third-order dispersive term $\mu \partial_x^3 u$, which spreads energy and favors shorter wavelengths. When these mechanisms achieve equilibrium, the equation admits solitary wave solutions—solitons—that propagate without change of form [2].

The KdV equation (29) possesses profound mathematical structure as a completely integrable Hamiltonian system. It admits an infinite hierarchy of conservation laws, the first three of which correspond to physically

meaningful quantities [28, 4]. The mass functional

$$M[u] = \int_{-\infty}^{\infty} u(x, t) dx \quad (30)$$

represents the total wave amplitude integrated over space. The momentum functional

$$P[u] = \int_{-\infty}^{\infty} u^2(x, t) dx \quad (31)$$

corresponds to the square-integrated field, related to wave action in the physical system. The energy functional

$$E[u] = \int_{-\infty}^{\infty} \left[\frac{\varepsilon}{2} u^3 - \frac{3\mu}{2} \left(\frac{\partial u}{\partial x} \right)^2 \right] dx \quad (32)$$

represents the Hamiltonian of the system, with the cubic term $\frac{\varepsilon}{2} u^3$ encoding nonlinear potential energy and the quadratic gradient term $-\frac{3\mu}{2} (\partial_x u)^2$ representing dispersive kinetic energy. These invariants (30)–(32) satisfy $dM/dt = 0$, $dP/dt = 0$, and $dE/dt = 0$ along solutions of equation (29), providing essential diagnostics for numerical accuracy [6].

The KdV equation (29) admits exact single-soliton solutions in the form [3]

$$u(x, t) = \frac{A}{\cosh^2 \left[\sqrt{\frac{\varepsilon A}{12\mu}} (x - x_0 - vt) \right]}, \quad (33)$$

where $A > 0$ denotes the soliton amplitude [m], x_0 represents the initial position [m], and the propagation velocity [m/s] is given by

$$v = \frac{\varepsilon A}{3}. \quad (34)$$

Equation (34) reveals the fundamental nonlinear dispersion relation: taller solitons travel faster, enabling overtaking collisions. The width parameter $w = \sqrt{12\mu/(\varepsilon A)}$ [m] characterizes the spatial extent, demonstrating that larger amplitudes produce narrower, faster solitons. The remarkable stability of these solutions under mutual collisions—emerging unchanged except for phase shifts—constitutes the defining characteristic of soliton behavior and validates the KdV equation as an integrable system [2, 5].

2.2 Numerical Implementation

The numerical solution of the KdV equation (29) requires spatial discretization of the differential operators and temporal integration of the resulting semi-discrete system. The **sangkuriang** solver employs the Fourier pseudo-spectral method for spatial derivatives [18, 19], which may provide exponential convergence rates for smooth periodic solutions, combined with adaptive high-order explicit time integration. This approach has been demonstrated to be effective for nonlinear dispersive wave equations [17, 8].

Consider a periodic spatial domain $x \in [x_{\min}, x_{\max}]$ with length $L = x_{\max} - x_{\min}$. We discretize this domain using N uniformly spaced grid points $x_j = x_{\min} + j\Delta x$ for $j = 0, 1, \dots, N - 1$, where the spatial resolution is $\Delta x = L/N$. Let $u_j(t) = u(x_j, t)$ denote the semi-discrete solution at grid point x_j and time t . The periodicity condition $u(x_{\min}, t) = u(x_{\max}, t)$ is implicitly enforced through the DFT representation. The DFT and its inverse are defined as [29]

$$\hat{u}_k = \frac{1}{N} \sum_{j=0}^{N-1} u_j \exp \left(-\frac{2\pi i k j}{N} \right), \quad k = 0, 1, \dots, N - 1, \quad (35)$$

$$u_j = \sum_{k=0}^{N-1} \hat{u}_k \exp \left(\frac{2\pi i k j}{N} \right), \quad j = 0, 1, \dots, N - 1, \quad (36)$$

where \hat{u}_k represents the k -th Fourier coefficient and $i = \sqrt{-1}$ denotes the imaginary unit. The computational implementation utilizes the FFT algorithm [30] available in NumPy [11], reducing the operation count from $\mathcal{O}(N^2)$ to $\mathcal{O}(N \log N)$ for both forward and inverse transforms.

The wavenumber vector corresponding to the DFT basis functions is given by

$$k_n = \begin{cases} \frac{2\pi n}{L}, & n = 0, 1, \dots, \lfloor N/2 \rfloor, \\ \frac{2\pi(n - N)}{L}, & n = \lceil N/2 \rceil, \dots, N - 1, \end{cases} \quad (37)$$

where the convention in equation (37) accounts for the standard FFT frequency ordering, with negative frequencies wrapped to the upper half of the index range. This wavenumber array can be efficiently generated using `numpy.fft.fftfreq` [11]. The spectral derivative operator acts on the Fourier coefficients through multiplication by ik_n . For the first-order spatial derivative, we have

$$\frac{\partial u}{\partial x}(x_j) = \text{IFFT}[ik_n \cdot \text{FFT}[u_j]] = \text{IFFT}[ik_n \hat{u}_k], \quad (38)$$

where `FFT[·]` and `IFFT[·]` denote the DFT (35) and its inverse (36), respectively. The third-order derivative

required for the dispersion term follows analogously:

$$\frac{\partial^3 u}{\partial x^3}(x_j) = \text{IFFT}[(ik_n)^3 \hat{u}_k]. \quad (39)$$

The real part of the inverse transform is extracted to eliminate numerical round-off errors in the imaginary component, which should theoretically vanish for real-valued solutions. This spectral differentiation approach is exact in the continuous limit and introduces errors only through aliasing in the nonlinear term, which can be controlled through sufficient spatial resolution [31].

Applying the spatial discretization described by equations (38) and (39) to the KdV equation (29), we obtain the semi-discrete ordinary differential equation (ODE) system

$$\frac{du_j}{dt} = F_j(\mathbf{u}(t)), \quad j = 0, 1, \dots, N-1, \quad (40)$$

where $\mathbf{u}(t) = [u_0(t), u_1(t), \dots, u_{N-1}(t)]^T \in \mathbb{R}^N$ denotes the state vector and the right-hand side operator is defined as

$$F_j(\mathbf{u}) = -\varepsilon u_j \left[\frac{\partial u}{\partial x} \right]_j - \mu \left[\frac{\partial^3 u}{\partial x^3} \right]_j. \quad (41)$$

The spatial derivatives in equation (41) are computed spectrally via equations (38) and (39). The nonlinear term $-\varepsilon u_j (\partial_x u)_j$ introduces quadratic coupling in Fourier space, which may lead to aliasing errors. However, for the resolutions employed in the `sangkuriang` test cases ($N = 512$ or $N = 1024$), these effects remain negligible relative to the specified tolerances [19].

The computational efficiency of the `sangkuriang` solver is significantly enhanced through JIT compilation and parallel processing capabilities provided by Numba [13], a dynamic compiler for Python that translates annotated numerical functions to optimized machine code via the Low Level Virtual Machine (LLVM) compiler infrastructure. The pointwise operations in the nonlinear and dispersive terms of equation (41) are implemented in specialized functions decorated with `@njit(parallel=True, cache=True)`, where the `parallel=True` flag enables automatic parallelization of loops across multiple Central Processing Unit (CPU) cores using Open Multi-Processing (OpenMP)-style threading [13]. Specifically, the elementwise computation of the nonlinear term $-\varepsilon u_j (\partial_x u)_j$ is structured using `prange` (parallel range) rather than Python's standard `range`, allowing Numba to distribute loop iterations across available processor threads. The `cache=True` option stores compiled machine code to disk, eliminating recompilation overhead in subsequent runs. The number of parallel threads is controlled via `numba.set_num_threads(n)`, where n may be specified by the user or defaults to the total number of available CPU cores detected by the operating system. This parallelization strategy exploits the embarrassingly parallel nature of pointwise arithmetic operations on grid data, though the actual performance gain depends on problem size, memory bandwidth, and hardware architecture—typical speedups range from $5\times$ to $50\times$ compared to interpreted NumPy operations for grid sizes $N \geq 512$ [13]. The JIT compilation overhead is amortized across multiple function calls during time integration, making the optimization particularly effective for the iterative RHS evaluations required by the adaptive time stepper. It should be noted that spectral derivative computations via FFT operations remain implemented in NumPy, as these already employ highly optimized Fastest Fourier Transform in the West (FFTW) or Intel Math Kernel Library (MKL) libraries that are difficult to improve upon with custom JIT compilation.

The semi-discrete system (40) is integrated in time using the DOP853 method [21, 32], an eighth-order explicit Runge–Kutta scheme with embedded fifth and third-order error estimators for adaptive step size control. This method is accessed through `scipy.integrate.solve_ivp` [12] with the `method='DOP853'` option. The DOP853 scheme requires twelve function evaluations per accepted step and provides local error estimates of the form [22]

$$\text{err}_{\text{local}} = \|\mathbf{u}_{n+1}^{(8)} - \mathbf{u}_{n+1}^{(5)}\|, \quad (42)$$

where $\mathbf{u}_{n+1}^{(8)}$ and $\mathbf{u}_{n+1}^{(5)}$ denote the eighth and fifth-order solution approximations at time t_{n+1} , respectively, and $\|\cdot\|$ represents an appropriately weighted norm. The step size adaptation follows the standard embedded method strategy [22]. If the error estimate (42) satisfies

$$\text{err}_{\text{local}} \leq \text{rtol} \cdot \|\mathbf{u}_{n+1}\| + \text{atol}, \quad (43)$$

where rtol denotes the relative tolerance and atol the absolute tolerance, the step is accepted and the next step size is computed as

$$\Delta t_{n+1} = 0.9 \Delta t_n \left(\frac{\text{rtol} \cdot \|\mathbf{u}_{n+1}\| + \text{atol}}{\text{err}_{\text{local}}} \right)^{1/8}, \quad (44)$$

where the exponent $1/8$ corresponds to the order of the method and the safety factor 0.9 provides robustness against step rejections. If condition (43) is violated, the step is rejected and recomputed with a reduced step size. The `sangkuriang` implementation employs default tolerances of $\text{rtol} = 10^{-10}$ and $\text{atol} = 10^{-12}$ for test cases 1–3, and tighter tolerances $\text{rtol} = 10^{-11}$ and $\text{atol} = 10^{-13}$ for the more complex three-soliton case 4.

The conservation properties described by equations (30)–(32) serve as critical diagnostics for numerical accuracy [33, 8]. For the semi-discrete solution $\mathbf{u}(t) = [u_0(t), u_1(t), \dots, u_{N-1}(t)]^T$, these integrals are approximated

using the composite trapezoidal rule [34]:

$$M(t) \approx \Delta x \sum_{j=0}^{N-1} u_j(t), \quad (45)$$

$$P(t) \approx \Delta x \sum_{j=0}^{N-1} u_j^2(t), \quad (46)$$

$$E(t) \approx \Delta x \sum_{j=0}^{N-1} \left[\frac{\varepsilon}{2} u_j^3(t) - \frac{3\mu}{2} \left(\frac{\partial u}{\partial x} \right)_j^2(t) \right], \quad (47)$$

where the spatial derivative in equation (47) is computed spectrally via equation (38). The trapezoidal rule achieves second-order accuracy for periodic functions [34], though the spectral accuracy of the solution itself may allow for higher-order quadrature. The computational implementation uses `numpy.trapz` [11] for numerical integration. The conservation errors are quantified as maximum relative deviations over the simulation time span $[0, T_{\text{final}}]$:

$$\text{err}_M = \max_{t \in [0, T_{\text{final}}]} \frac{|M(t) - M(0)|}{|M(0)|}, \quad (48)$$

$$\text{err}_P = \max_{t \in [0, T_{\text{final}}]} \frac{|P(t) - P(0)|}{|P(0)|}, \quad (49)$$

$$\text{err}_E = \max_{t \in [0, T_{\text{final}}]} \frac{|E(t) - E(0)|}{|E(0)|}. \quad (50)$$

These metrics provide quantitative measures of the numerical method's ability to preserve the underlying geometric structure of the KdV equation. Conservation errors below 10^{-2} are generally considered acceptable for practical simulations, though the `sangkuriang` implementation typically achieves errors in the range 10^{-6} to 10^{-4} depending on the test case complexity [36].

The complete numerical algorithm proceeds as follows. Given initial condition $u_0(x) = u(x, t = 0)$, we sample at grid points to obtain the initial state vector $\mathbf{u}(0) = [u_0(x_0), u_0(x_1), \dots, u_0(x_{N-1})]^T$. The wavenumber vector $\{k_n\}_{n=0}^{N-1}$ is precomputed according to equation (37) and stored for repeated use in spectral derivative evaluations. The Numba JIT compiler is initialized with the specified number of parallel threads via `set_num_threads(n_cores)`, enabling multi-core parallelization for subsequent RHS evaluations. At each time step, the right-hand side operator (41) is evaluated by: (i) computing the FFT of the current state via equation (35), (ii) multiplying by ik_n and $(ik_n)^3$ to obtain derivative Fourier coefficients, (iii) applying the IFFT via equation (36) to recover physical space derivatives, and (iv) assembling the nonlinear and dispersive terms using JIT-compiled parallel functions. The DOP853 integrator advances the solution from t_n to t_{n+1} according to the adaptive strategy described by equations (43)–(44). At specified output times $\{t_m\}_{m=0}^M$, the solution state is stored and conservation laws (45)–(47) are evaluated for diagnostic purposes. This process continues until the final time T_{final} is reached. The `sangkuriang` numerical implementation leverages established scientific computing libraries: NumPy [11] for array operations and FFT routines, SciPy [12] for adaptive ODE integration, Numba [13] for JIT compilation and parallel processing optimization, Matplotlib [35] for visualization, and netCDF4 [23] for scientific data output following CF-1.8 conventions. This combination of spectral methods, high-order adaptive time integration, and parallel computing optimizations may provide both computational efficiency and numerical accuracy appropriate for research-grade simulations of soliton dynamics.

2.3 Numerical Experiments

The `sangkuriang` solver implementation is validated and demonstrated through four progressively complex test cases that probe different aspects of KdV soliton dynamics. These scenarios are designed to assess: (i) baseline propagation characteristics of isolated solitons, (ii) interaction dynamics between equal-amplitude waves, (iii) overtaking collision phenomena arising from amplitude-dependent velocities, and (iv) complex multi-body interactions in three-soliton systems. While the `sangkuriang` framework is general and may be applied to arbitrary initial conditions satisfying the periodicity constraint, these canonical test cases provide standardized benchmarks that have been extensively studied in the literature [2, 6, 3] and serve to verify the implementation's ability to capture the essential physics of nonlinear dispersive wave propagation.

The first test case examines the propagation of a single soliton in isolation, serving as a baseline reference for subsequent multi-soliton scenarios. The initial condition is specified using the exact single-soliton solution profile (33) in the form

$$u(x, 0) = \frac{A}{\cosh^2 \left[\frac{x-x_0}{w} \right]}, \quad (51)$$

with amplitude $A = 4.0$ m, width parameter $w = 2.0$ m, and initial position $x_0 = -10.0$ m. The computational domain spans $x \in [-30, 30]$ m discretized with $N = 512$ grid points, providing spatial resolution $\Delta x \approx 0.117$ m. The physical parameters are set to $\mu = 0.1$ m³/s and $\varepsilon = 0.2$ m⁻¹, yielding theoretical propagation velocity $v = \varepsilon A / 3 \approx 0.267$ m/s according to equation (34). The simulation extends to final time $T_{\text{final}} = 50.0$ s,

during which the soliton should traverse approximately 13.3 m while maintaining its shape. This test case validates the `sangkuriang` solver's ability to preserve soliton structure over extended propagation distances and provides a baseline for assessing conservation law preservation. The expected relative conservation errors for mass, momentum, and energy should remain below 10^{-6} for this smooth, non-interacting solution [33].

The second test case investigates the interaction between two solitons of equal amplitude, which may exhibit phase shift phenomena without energy exchange. The initial condition comprises a linear superposition of two sech^2 profiles:

$$u(x, 0) = \frac{A_1}{\cosh^2 \left[\frac{x-x_1}{w_1} \right]} + \frac{A_2}{\cosh^2 \left[\frac{x-x_2}{w_2} \right]}, \quad (52)$$

with identical amplitudes $A_1 = A_2 = 3.0$ m, widths $w_1 = w_2 = 2.0$ m, and symmetrically positioned at $x_1 = -15.0$ m and $x_2 = 15.0$ m. The domain is extended to $x \in [-40, 40]$ m with $N = 512$ points ($\Delta x \approx 0.156$ m), and the simulation time increased to $T_{\text{final}} = 60.0$ s. Since both solitons possess equal amplitudes, they propagate with identical velocities $v = 0.2$ m/s and thus maintain constant separation. However, the initial linear superposition (52) is not an exact solution of the nonlinear KdV equation, necessitating an adjustment phase during which the wave profiles redistribute energy into soliton modes and dispersive radiation [6]. This test case assesses the `sangkuriang` solver's handling of multi-soliton configurations and the emergence of approximate two-soliton solutions from non-exact initial data. The symmetric configuration also serves as a diagnostic for numerical artifacts, as any asymmetry in the computed solution would indicate spatial discretization errors or inadequate time integration accuracy.

The third test case examines the overtaking collision between solitons of unequal amplitudes, demonstrating the remarkable elastic scattering property that defines soliton behavior. The initial condition takes the form of equation (52) with asymmetric parameters: $A_1 = 6.0$ m, $w_1 = 1.5$ m, $x_1 = -18.0$ m for the leading (taller) soliton, and $A_2 = 2.0$ m, $w_2 = 2.5$ m, $x_2 = -5.0$ m for the trailing (shorter) soliton. According to the velocity relation (34), the taller soliton propagates at $v_1 = 0.4$ m/s while the shorter moves at $v_2 \approx 0.133$ m/s, ensuring that the faster wave overtakes the slower one during the simulation. The domain spans $x \in [-40, 40]$ m with $N = 512$ points, and the final time is extended to $T_{\text{final}} = 70.0$ s to observe the complete collision sequence and subsequent separation. This scenario probes the nonlinear interaction dynamics most severely, as the collision involves significant amplitude modulation and temporary waveform distortion [2]. The remarkable theoretical prediction—that both solitons emerge from the collision with their original amplitudes and velocities intact, differing only by phase shifts—provides a stringent test of the numerical method's ability to capture the integrable structure of the KdV equation [5]. Conservation errors may increase during the collision phase due to enhanced nonlinearity, but should remain below 10^{-4} for the employed tolerances.

The fourth test case extends the complexity to a three-soliton system, creating a choreography of multiple interactions that tests the `sangkuriang` solver's robustness under more challenging conditions. The initial condition generalizes equation (52) to three components:

$$u(x, 0) = \sum_{j=1}^3 \frac{A_j}{\cosh^2 \left[\frac{x-x_j}{w_j} \right]}, \quad (53)$$

with amplitudes $A_1 = 7.0$ m, $A_2 = 4.0$ m, $A_3 = 2.5$ m, widths $w_1 = 1.2$ m, $w_2 = 1.8$ m, $w_3 = 2.2$ m, and initial positions $x_1 = -25.0$ m, $x_2 = -10.0$ m, $x_3 = 5.0$ m, respectively. The corresponding velocities are $v_1 \approx 0.467$ m/s, $v_2 \approx 0.267$ m/s, and $v_3 \approx 0.167$ m/s, ordered such that each faster soliton will sequentially overtake the slower ones ahead. To accommodate the increased spatial extent of the three-wave system and provide adequate resolution for the narrowest soliton, the domain is enlarged to $x \in [-50, 50]$ m with enhanced resolution $N = 1024$ ($\Delta x \approx 0.098$ m). The simulation extends to $T_{\text{final}} = 80.0$ s with tightened tolerances $\text{rtol} = 10^{-11}$ and $\text{atol} = 10^{-13}$ to maintain accuracy through multiple collision events. This test case may exhibit complex interaction patterns including transient amplitude amplifications during collisions, the generation of small-amplitude dispersive radiation, and intricate phase shift accumulations [6, 3]. The successful navigation of these multiple interactions while preserving conservation laws and soliton identities demonstrates the `sangkuriang` solver's capability for research-grade simulations of multi-soliton dynamics.

The physical parameters $\mu = 0.1$ m³/s and $\varepsilon = 0.2$ m⁻¹ are held constant across all test cases to facilitate direct comparison of dynamical behaviors. These values are representative of shallow water wave systems and ensure that the balance between nonlinearity and dispersion falls within the regime where soliton solutions are well-defined [26]. The specific choices of soliton amplitudes and positions in each test case are informed by established benchmarks in the soliton literature [2, 20] and are designed to produce qualitatively distinct interaction scenarios within computationally tractable simulation times. While these four cases provide comprehensive validation of the `sangkuriang` solver's core functionality, the implementation supports arbitrary initial conditions through the `SechProfile`, `TanhProfile`, `GaussianProfile`, and `MultiSoliton` classes, enabling users to investigate alternative scenarios such as soliton generation from non-sech² initial data, wave packet decomposition, or soliton interactions with continuous wave backgrounds.

The output from each `sangkuriang` simulation includes the complete spatiotemporal field $u(x, t)$, conservation law time series $M(t)$, $P(t)$, $E(t)$ as defined in equations (45)–(47), relative conservation errors (48)–(50), and diagnostic information regarding computational cost (number of function evaluations, wall clock time). Data are stored in netCDF4 format [23] following CF-1.8 metadata conventions, facilitating interoperability with

standard scientific data analysis tools. Animated visualizations are generated showing the evolving wave profile in three-dimensional space-time representations, with conservation law diagnostics overlaid to provide immediate visual feedback on solution quality. These outputs enable both qualitative assessment of soliton dynamics and quantitative verification of the numerical implementation's fidelity to the underlying physics encoded in the KdV equation (29).

2.4 Data Analysis

The diagnostic analysis of simulation outputs is performed independently of the `sangkuriang` solver library through a dedicated suite of post-processing routines implemented in Python. These routines employ NumPy [11] for array operations and FFT, SciPy [12] for signal processing and distance computations, and Matplotlib [35] for visualization. Simulation data archived in netCDF4 format [23] following CF-1.8 conventions are subjected to four complementary analyses: verification of conservation law preservation, soliton trajectory tracking with velocity validation, spectral information-theoretic characterization, and phase space recurrence quantification. Each analysis extracts quantitative metrics that collectively assess both numerical accuracy and physical fidelity of the computed solutions.

The conservation analysis quantifies the temporal stability of the three KdV invariants defined in equations (45)–(47). Let $Q(t)$ denote any of the conserved quantities $M(t)$, $P(t)$, or $E(t)$ evaluated at discrete output times $\{t_n\}_{n=0}^{N_t-1}$, where N_t is the total number of stored time snapshots. The instantaneous relative deviation from the initial state is defined as

$$\delta_Q(t_n) = \frac{Q(t_n) - Q(t_0)}{|Q(t_0)|}, \quad (54)$$

which measures the fractional departure of Q from its initial value $Q(t_0) = Q_0$. Three statistical measures characterize the behavior of δ_Q over the simulation interval. The maximum relative error,

$$\text{err}_Q = \max_{0 \leq n < N_t} |\delta_Q(t_n)|, \quad (55)$$

captures the worst-case deviation and is stored directly in the netCDF output files. The RMS error,

$$\sigma_Q = \left[\frac{1}{N_t} \sum_{n=0}^{N_t-1} \delta_Q^2(t_n) \right]^{1/2}, \quad (56)$$

provides a time-averaged measure of conservation fidelity that is less sensitive to isolated outliers. To distinguish systematic drift from bounded oscillations, the linear drift rate γ_Q is extracted via ordinary least-squares regression. Defining the design matrix $\mathbf{A} \in \mathbb{R}^{N_t \times 2}$ with elements $A_{n1} = t_n$ and $A_{n2} = 1$, and the observation vector $\mathbf{b} = [\delta_Q(t_0), \delta_Q(t_1), \dots, \delta_Q(t_{N_t-1})]^T$, the drift rate is obtained as the first component of the least-squares solution

$$[\gamma_Q, \beta_Q]^T = (\mathbf{A}^T \mathbf{A})^{-1} \mathbf{A}^T \mathbf{b}, \quad (57)$$

where β_Q is an intercept term. A nonzero γ_Q [s^{-1}] indicates secular accumulation of numerical error, whereas $\gamma_Q \approx 0$ with finite σ_Q suggests oscillatory but bounded deviations consistent with symplectic or near-symplectic integration.

Soliton trajectory extraction proceeds through systematic identification and tracking of local amplitude maxima in the spatiotemporal field $u(x_j, t_n)$. At each output time t_n , the discrete spatial profile $\{u_j^{(n)}\}_{j=0}^{N-1} \equiv \{u(x_j, t_n)\}_{j=0}^{N-1}$ is analyzed using the `scipy.signal.find_peaks` routine [12], which identifies indices j^* satisfying $u_{j^*}^{(n)} > u_{j^*-1}^{(n)}, u_{j^*}^{(n)} > u_{j^*+1}^{(n)}$, subject to additional constraints. Two filtering parameters govern peak selection: a height threshold u_{th} requiring $u_{j^*}^{(n)} > u_{\text{th}}$, and a minimum separation distance d_{min} (in grid points) enforcing $|j_1^* - j_2^*| > d_{\text{min}}$ between distinct peaks. For the test cases examined, $u_{\text{th}} = 0.5$ m for multi-soliton configurations and $u_{\text{th}} = 1.0$ m for single-soliton runs, with $d_{\text{min}} = 10$ grid points throughout. Each detected peak yields a triplet $(t_n, x_{j^*}, u_{j^*}^{(n)})$ recording the time, spatial position, and amplitude.

For configurations containing K solitons, individual trajectories must be disambiguated from the aggregate peak data. This is accomplished through amplitude-based sorting at each time instant: letting $\{(x_k^{(n)}, A_k^{(n)})\}_{k=1}^{K_n}$ denote the K_n peaks detected at time t_n with positions $x_k^{(n)}$ and amplitudes $A_k^{(n)}$, these are reordered such that $A_1^{(n)} \geq A_2^{(n)} \geq \dots \geq A_{K_n}^{(n)}$. The k -th soliton track is then defined as the sequence $\{(t_n, x_k^{(n)})\}$ across all times where at least k peaks were detected. This ranking scheme exploits the amplitude-velocity ordering inherent to KdV solitons: since taller solitons propagate faster according to equation (34), amplitude rank provides a consistent identifier even through collision events where spatial ordering temporarily inverts.

The propagation velocity of each tracked soliton is determined by linear regression of position against time. For the k -th soliton trajectory restricted to a temporal window $[t_a, t_b]$ containing N_k data points, the measured velocity v_k^{meas} minimizes the sum of squared residuals:

$$v_k^{\text{meas}} = \arg \min_v \sum_{n: t_n \in [t_a, t_b]} \left[x_k^{(n)} - vt_n - x_k^{(0)} \right]^2. \quad (58)$$

The explicit solution via `numpy.polyfit` [11] yields v_k^{meas} as the slope of the fitted line $x_k(t) = v_k^{\text{meas}}t + x_k^{(0)}$.

Goodness-of-fit is quantified by the coefficient of determination

$$R_k^2 = 1 - \frac{\sum_n (x_k^{(n)} - v_k^{\text{meas}} t_n - x_k^{(0)})^2}{\sum_n (x_k^{(n)} - \bar{x}_k)^2}, \quad (59)$$

where $\bar{x}_k = N_k^{-1} \sum_n x_k^{(n)}$ is the mean position. Values $R_k^2 \rightarrow 1$ indicate linear trajectories consistent with constant-velocity propagation. The mean soliton amplitude over the fitting interval,

$$\bar{A}_k = \frac{1}{N_k} \sum_{n: t_n \in [t_a, t_b]} A_k^{(n)}, \quad (60)$$

together with its standard deviation σ_{A_k} , enables comparison against the theoretical velocity relation (34). The theoretical prediction $v_k^{\text{theo}} = \varepsilon \bar{A}_k / 3$ should match v_k^{meas} for well-resolved soliton solutions, providing validation of both numerical accuracy and the soliton character of computed waveforms.

Spectral analysis employs the DFT (35) to characterize the wavenumber content of each spatial snapshot. For the field $\{u_j^{(n)}\}_{j=0}^{N-1}$ at time t_n , the power spectral density is computed as

$$P_m^{(n)} = \frac{1}{N} |\hat{u}_m^{(n)}|^2, \quad m = 0, 1, \dots, N-1, \quad (61)$$

where $\hat{u}_m^{(n)}$ denotes the m -th Fourier coefficient obtained via `numpy.fft.fft` [11]. The corresponding wavenumbers k_m follow from equation (37) and are generated using `numpy.fft.fftfreq`. Normalization of the power spectrum yields a discrete probability distribution over wavenumber space:

$$p_m^{(n)} = \frac{P_m^{(n)}}{\sum_{\ell=0}^{N-1} P_{\ell}^{(n)}}, \quad \sum_{m=0}^{N-1} p_m^{(n)} = 1, \quad (62)$$

representing the fractional energy content at wavenumber k_m . This spectral probability distribution forms the basis for three information-theoretic measures that characterize distinct aspects of the wave field structure.

The spectral entropy [37] quantifies the breadth of spectral energy distribution through the normalized Shannon entropy of $\{p_m^{(n)}\}$:

$$S_k^{(n)} = -\frac{1}{\ln N} \sum_{m=0}^{N-1} p_m^{(n)} \ln p_m^{(n)}, \quad (63)$$

where terms with $p_m^{(n)} < 10^{-15}$ are excluded from the summation to avoid numerical singularities. The normalization by $\ln N$ ensures $S_k^{(n)} \in [0, 1]$, with $S_k^{(n)} = 0$ corresponding to a monochromatic signal (all energy concentrated at a single wavenumber) and $S_k^{(n)} = 1$ to uniform spectral distribution (white noise). Soliton profiles, characterized by smooth sech² envelopes with exponentially decaying Fourier spectra, exhibit intermediate entropy values that remain approximately constant during propagation.

The López–Ruiz–Mancini–Calbet (LMC) statistical complexity [38] captures the interplay between disorder and departure from equilibrium through the product

$$C_{\text{LMC}}^{(n)} = H^{(n)} \times D^{(n)}, \quad (64)$$

where $H^{(n)} = S_k^{(n)}$ is the normalized spectral entropy defined in equation (63), and the disequilibrium

$$D^{(n)} = \sum_{m=0}^{N-1} \left(p_m^{(n)} - \frac{1}{N} \right)^2 \quad (65)$$

measures the squared Euclidean distance between the observed distribution $\{p_m^{(n)}\}$ and the uniform distribution $\{1/N\}$. This construction ensures $C_{\text{LMC}}^{(n)} = 0$ for both perfectly ordered states ($H^{(n)} = 0$, all energy at one mode) and maximally disordered states ($D^{(n)} = 0$, uniform distribution), attaining nonzero values only for intermediate configurations exhibiting nontrivial structure [38]. The LMC complexity thus distinguishes structured nonequilibrium states from both trivial order and featureless randomness.

The Fisher information [39, 40, 41] provides a complementary characterization of spatial localization by measuring the “sharpness” of the amplitude distribution. Defining the normalized spatial probability density

$$\rho_j^{(n)} = \frac{|u_j^{(n)}| + \epsilon_{\text{reg}}}{\sum_{\ell=0}^{N-1} (|u_{\ell}^{(n)}| + \epsilon_{\text{reg}}) \Delta x}, \quad (66)$$

where $\epsilon_{\text{reg}} = 10^{-15}$ is a regularization parameter preventing division by zero, the discrete Fisher information is computed as

$$F^{(n)} = \sum_{j=0}^{N-1} \frac{1}{\rho_j^{(n)}} \left(\frac{\partial \rho}{\partial x} \Big|_j \right)^2 \Delta x. \quad (67)$$

The spatial derivative $(\partial_x \rho)_j^{(n)}$ is evaluated using second-order central differences via `numpy.gradient` [11]:

$$\frac{\partial \rho}{\partial x} \Big|_j^{(n)} \approx \frac{\rho_{j+1}^{(n)} - \rho_{j-1}^{(n)}}{2\Delta x}, \quad (68)$$

with one-sided differences at domain boundaries. Higher Fisher information indicates sharper spatial gradients and hence more localized wave structures; for soliton solutions, $F^{(n)}$ scales inversely with the characteristic width parameter w appearing in equation (33). During soliton collisions, transient increases in $F^{(n)}$ reflect the temporary steepening of gradients as wave profiles overlap.

Phase space analysis employs recurrence quantification analysis (RQA) [42, 43] to characterize the dynamical structure of simulation trajectories. For integrable Hamiltonian systems possessing multiple conservation laws, trajectories are confined to low-dimensional invariant manifolds in the full phase space; deviations from this structure would indicate either numerical error or departure from integrability. The analysis proceeds by embedding the temporal evolution in a three-dimensional conservation space with coordinates

$$\mathbf{y}^{(n)} = \left(\frac{M(t_n)}{M_0}, \frac{P(t_n)}{P_0}, \frac{E(t_n)}{E_0} \right)^T \in \mathbb{R}^3, \quad (69)$$

where normalization by initial values M_0 , P_0 , E_0 renders the components dimensionless and of comparable magnitude. For a perfectly conservative numerical scheme, $\mathbf{y}^{(n)} = (1, 1, 1)^T$ for all n ; deviations from this ideal point trace out a trajectory reflecting cumulative numerical errors.

The pairwise Euclidean distance matrix $\mathbf{D} \in \mathbb{R}^{N_t \times N_t}$ with elements

$$D_{ij} = \|\mathbf{y}^{(i)} - \mathbf{y}^{(j)}\| = \left[\sum_{\alpha=1}^3 (y_{\alpha}^{(i)} - y_{\alpha}^{(j)})^2 \right]^{1/2} \quad (70)$$

is computed efficiently using `scipy.spatial.distance.pdist` and `squareform` [12]. A recurrence threshold ε is determined adaptively as the q -th percentile of the nonzero elements of \mathbf{D} , with $q = 10\text{--}15$ providing robust results across test cases. The binary recurrence matrix [42] is then constructed as

$$R_{ij} = \Theta(\varepsilon - D_{ij}) = \begin{cases} 1, & D_{ij} < \varepsilon, \\ 0, & D_{ij} \geq \varepsilon, \end{cases} \quad (71)$$

where $\Theta(\cdot)$ denotes the Heaviside step function. By construction, $R_{ii} = 1$ for all i (self-recurrence), and $R_{ij} = R_{ji}$ (symmetry).

Two scalar metrics extracted from the recurrence matrix characterize the dynamical behavior. The recurrence rate

$$\text{RR} = \frac{1}{N_t(N_t - 1)} \sum_{\substack{i,j=0 \\ i \neq j}}^{N_t-1} R_{ij} \quad (72)$$

quantifies the density of recurrent pairs, excluding the trivial diagonal $i = j$. Higher RR indicates that the trajectory repeatedly visits similar regions of conservation space, consistent with bounded oscillatory errors rather than secular drift. The determinism

$$\text{DET} = \frac{\sum_{\ell \geq \ell_{\min}} \ell \cdot P(\ell)}{\sum_{i \neq j} R_{ij}} \quad (73)$$

measures the fraction of recurrence points forming diagonal line structures of length at least ℓ_{\min} (typically $\ell_{\min} = 2$). Here $P(\ell)$ denotes the number of diagonal lines of exactly length ℓ in the recurrence matrix, where a diagonal line at offset $k > 0$ consists of consecutive entries $R_{i,i+k} = R_{i+1,i+1+k} = \dots = 1$. Diagonal structures arise when segments of the trajectory evolve in parallel, a hallmark of deterministic dynamics on regular (non-chaotic) attractors [43]. For integrable systems such as the KdV equation, $\text{DET} \rightarrow 1$ reflects confinement to invariant tori, whereas chaotic systems exhibit $\text{DET} \ll 1$ due to sensitive dependence on initial conditions disrupting parallel trajectory segments.

Complementary phase space characterization is obtained through analysis of Fourier mode amplitudes. The leading K complex Fourier coefficients $\{\hat{u}_m^{(n)}\}_{m=0}^{K-1}$ (typically $K = 3\text{--}5$) extracted from each temporal snapshot define a trajectory in a $2K$ -dimensional space (accounting for real and imaginary parts). Projection onto the real components of the first two modes, $(\text{Re}[\hat{u}_0^{(n)}], \text{Re}[\hat{u}_1^{(n)}])$, yields a two-dimensional phase portrait that visualizes the modal dynamics. For the KdV equation, the zeroth mode $\hat{u}_0^{(n)} = N^{-1} \sum_j u_j^{(n)}$ is proportional to the spatial mean (and hence to the mass M), while higher modes capture spatial structure. Bounded, closed orbits in this projection confirm the quasi-periodic character expected of integrable dynamics, whereas space-filling or divergent trajectories would signal chaotic or unstable behavior.

3 Results and Discussion

The `sangkuriang` solver was validated through four test cases of increasing complexity, executed on a laptop-class workstation (Lenovo ThinkPad P52s with Intel Core i7-8550U processor at 4.0 GHz, 8 logical cores) running

Fedora Linux 39 (kernel 6.11.9-100.fc39.x86_64). This hardware configuration represents a modest computational platform, permitting assessment of the solver’s practical utility for research applications without access to high-performance computing resources.

Table 1 summarizes the computational cost for each test case. The single-soliton simulation (Case 1) required 208,202 adaptive time steps to integrate over the 50 s interval, completing in approximately 152 s of wall-clock time. The adaptive time stepper selected finer temporal resolution for this case due to the smaller spatial domain ($L = 60$ m) and correspondingly higher wavenumber content relative to Cases 2 and 3. The two equal-amplitude soliton simulation (Case 2) completed in 75.7 s using 98,612 steps, while the overtaking collision (Case 3) required 115,658 steps and 87.6 s. The three-soliton configuration (Case 4), employing doubled spatial resolution ($N = 1024$) and tightened tolerances ($\text{rtol} = 10^{-11}$, $\text{atol} = 10^{-13}$), demanded 551,858 steps and 534 s of computation time. These timings suggest that the Numba-accelerated implementation achieves reasonable throughput for exploratory research, though the scaling with grid resolution and tolerance warrants consideration for production simulations.

Table 1: Computational performance metrics for the four test cases. All simulations employed 8 parallel threads via Numba JIT compilation.

| Case | N | Δx [m] | T_{final} [s] | Steps | CPU time [s] | Steps/s |
|--------------------|------|----------------|------------------------|---------|--------------|---------|
| 1 (Single soliton) | 512 | 0.117 | 50 | 208,202 | 152.0 | 1370 |
| 2 (Two equal) | 512 | 0.157 | 60 | 98,612 | 75.7 | 1303 |
| 3 (Collision) | 512 | 0.157 | 70 | 115,658 | 87.6 | 1320 |
| 4 (Three solitons) | 1024 | 0.098 | 80 | 551,858 | 534.4 | 1033 |

The throughput, measured in time steps per second, remained relatively consistent across Cases 1–3 at approximately 1300–1370 steps/s, decreasing to roughly 1030 steps/s for Case 4. This reduction likely reflects the increased memory bandwidth demands associated with the larger grid and the superlinear scaling of FFT operations, which nominally follow $\mathcal{O}(N \log N)$ complexity [30]. Nevertheless, all simulations completed within times amenable to interactive research workflows.

The preservation of the three KdV invariants—mass M , momentum P , and energy E as defined in equations (45)–(47)—provides a stringent test of numerical accuracy. Figure 2 displays the temporal evolution of relative conservation errors for all test cases.

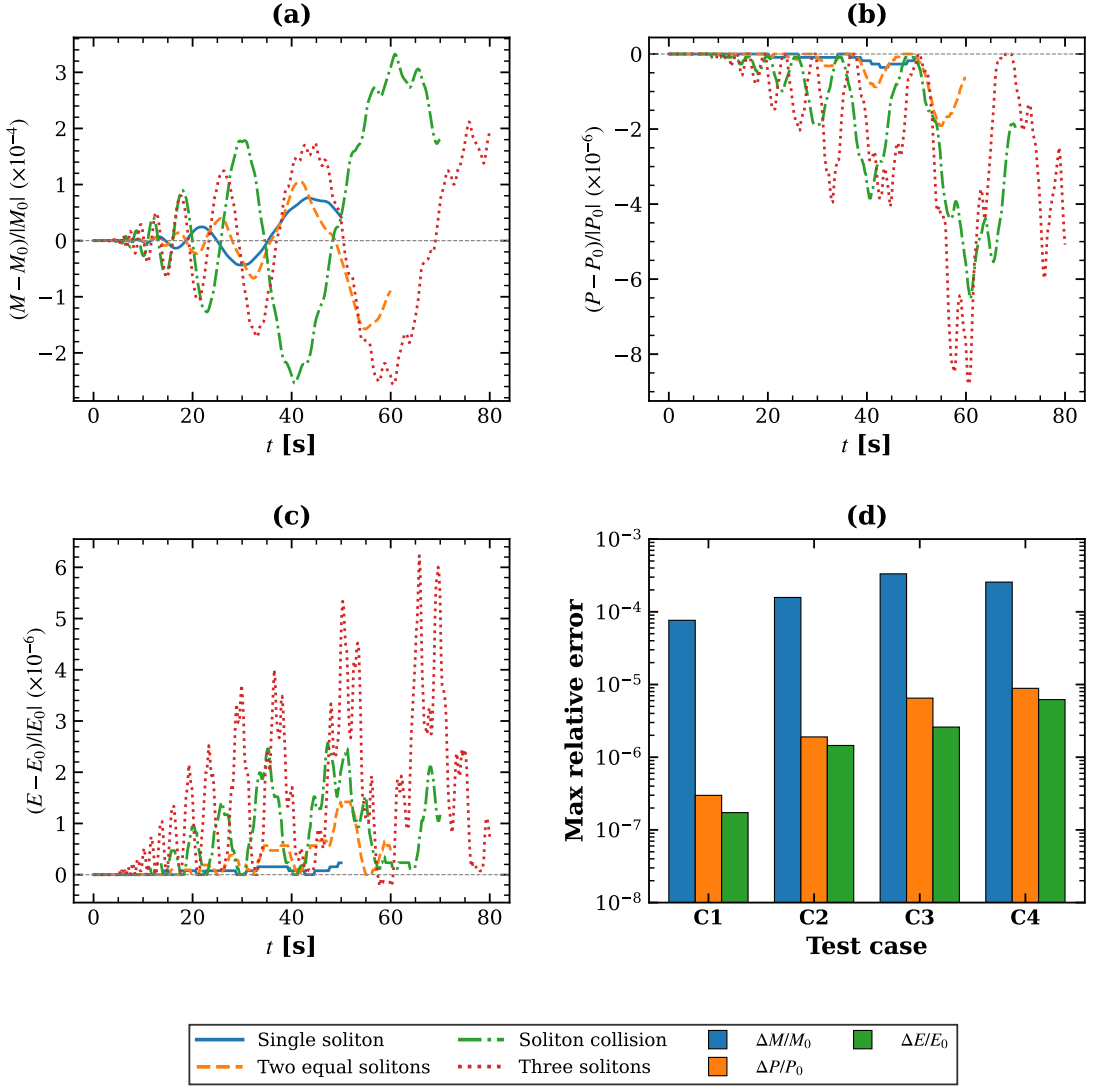


Figure 2: Conservation law diagnostics. (a) Relative mass deviation $(M - M_0)/|M_0|$; (b) relative momentum deviation $(P - P_0)/|P_0|$; (c) relative energy deviation $(E - E_0)/|E_0|$; (d) maximum relative errors across all cases on logarithmic scale. Solid blue: single soliton (C1); dashed orange: two equal solitons (C2); dash-dotted green: soliton collision (C3); dotted red: three solitons (C4).

The single-soliton case exhibited the smallest conservation errors, with maximum relative deviations of 7.64×10^{-5} for mass, 2.98×10^{-7} for momentum, and 1.73×10^{-7} for energy. These values are consistent with the specified integration tolerances and confirm that the pseudo-spectral spatial discretization introduces negligible additional error for smooth, non-interacting solutions. The root-mean-square (RMS) errors were approximately half the maximum values (3.55×10^{-5} , 1.30×10^{-7} , and 8.28×10^{-8} , respectively), indicating that the deviations represent bounded oscillations rather than secular drift. Linear regression of the conservation time series yielded drift rates on the order of 10^{-9} s^{-1} for momentum and energy, suggesting that the dominant error contribution arises from the non-symplectic character of the DOP853 integrator rather than from systematic bias [22].

Multi-soliton configurations exhibited moderately larger conservation errors, as anticipated from the increased solution complexity during interaction events. The two equal-amplitude soliton case (Case 2) showed maximum errors of 1.57×10^{-4} (mass), 1.90×10^{-6} (momentum), and 1.45×10^{-6} (energy). The overtaking collision (Case 3) produced the largest mass error at 3.33×10^{-4} , with momentum and energy errors of 6.49×10^{-6} and 2.60×10^{-6} , respectively. Figure 2(a)–(c) reveals that the conservation deviations exhibit transient excursions correlated with collision events, particularly evident in the three-soliton case where multiple interactions occur. Despite the increased complexity of Case 4, the maximum errors (2.56×10^{-4} , 8.86×10^{-6} , 6.20×10^{-6}) remained comparable to or smaller than those of Case 3, likely reflecting the benefits of enhanced spatial resolution and tighter tolerances employed for this configuration.

The bar chart in Figure 2(d) presents a comparative summary of maximum relative errors across all cases. A consistent hierarchy emerges: mass conservation errors exceed momentum errors by approximately two orders of magnitude, which in turn exceed energy errors. This ordering may reflect the different sensitivities of each integral to high-wavenumber components of the solution, with the energy functional (32) involving spatial derivatives

that weight the well-resolved low-wavenumber content more heavily. Across all test cases, the conservation errors remain well below the 10^{-2} threshold commonly adopted as acceptable for practical simulations of Hamiltonian systems [36], suggesting that the `sangkuriang` implementation maintains adequate fidelity to the underlying physics.

Figure 3 presents three-dimensional visualizations of the wave field $u(x, t)$ for each test case, rendered with consistent axis limits ($x \in [-50, 50]$ m, $t \in [0, 80]$ s, $u \in [0, 9]$ m) to facilitate direct comparison.

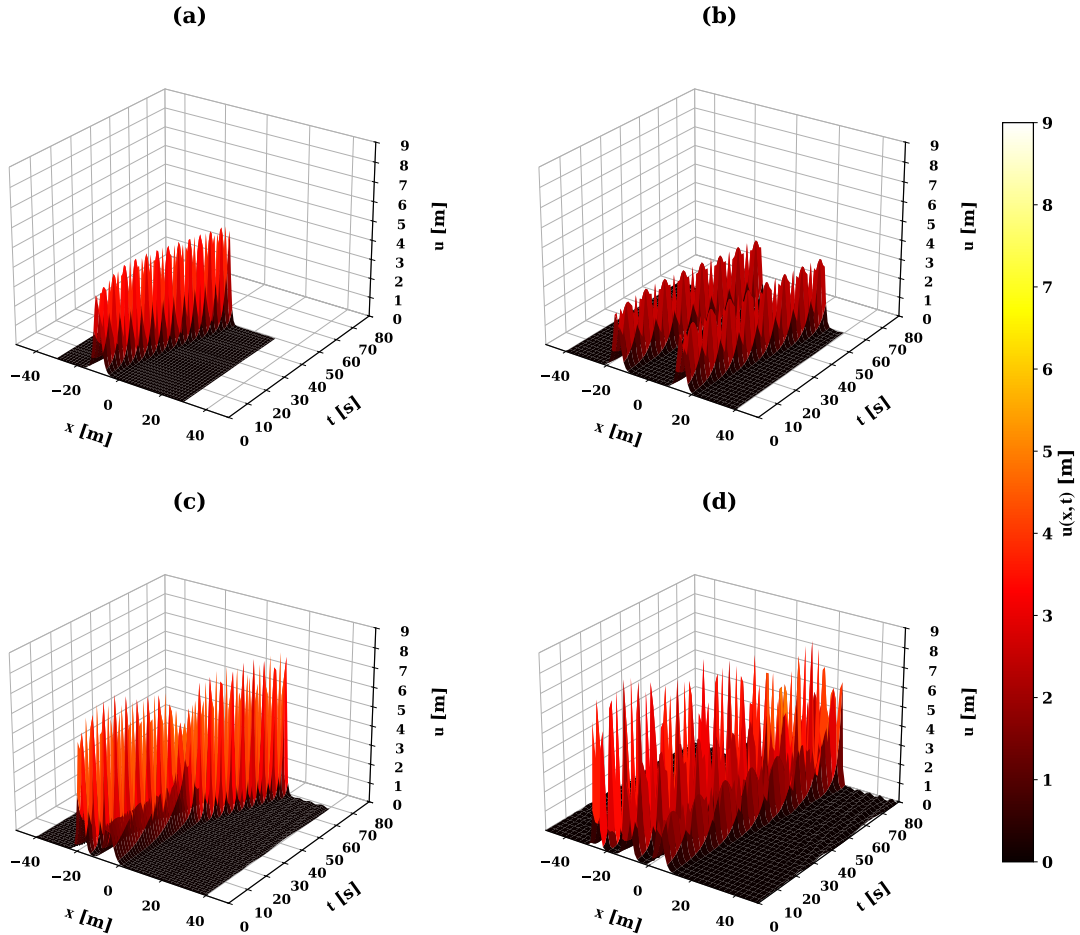


Figure 3: Three-dimensional spatiotemporal evolution of the wave amplitude $u(x, t)$ for the four test cases. (a) Single soliton propagating rightward; (b) two equal-amplitude solitons; (c) overtaking collision between fast (tall) and slow (short) solitons; (d) three-soliton interaction. Color scale indicates amplitude in meters. View angles: elevation 25° , azimuth -55° .

Panel (a) illustrates the single-soliton case, where the initial sech^2 profile propagates from left to right while maintaining its characteristic shape. The wave amplitude increases slightly from the initial value of approximately 4.0 m to a final peak of 5.2 m, with a global maximum of 5.21 m observed during the simulation. This amplitude evolution reflects the adjustment of the initial condition—which approximates but does not precisely match the exact soliton solution (33)—toward a true soliton state through radiation of small-amplitude dispersive waves [6]. The peak position advanced by 17.8 m over the 50 s integration interval, corresponding to an average velocity of 0.357 m/s.

The two equal-amplitude soliton configuration, shown in panel (b), exhibits parallel propagation of two $A = 3.0$ m solitons initially separated by 30 m. Since the KdV soliton velocity is proportional to amplitude according to equation (34), these waves maintain constant separation throughout the simulation. The surface plot reveals two distinct ridges traversing the space-time domain without intersection, confirming the expected kinematic behavior. Minor amplitude variations (final peak 3.66 m versus initial 3.0 m) again indicate adjustment toward exact soliton profiles.

Panel (c) displays the overtaking collision scenario, which constitutes the most stringent test of the solver's ability to capture nonlinear interaction dynamics. The taller soliton ($A_1 = 6.0$ m), propagating faster than the shorter wave ($A_2 = 2.0$ m), overtakes and passes through it near $t \approx 35$ s and $x \approx 0$ m. The characteristic "X"-shaped intersection pattern in the space-time surface demonstrates the elastic scattering property of KdV solitons: both waves emerge from the collision with their identities intact, differing only by phase shifts [2]. The global maximum amplitude of 7.55 m, exceeding the linear superposition of the two initial amplitudes, reflects the transient nonlinear amplification during the collision phase.

The three-soliton interaction in panel (d) presents the most complex dynamics, with multiple collision events occurring as the fastest soliton ($A_1 = 7.0$ m) successively overtakes the intermediate ($A_2 = 4.0$ m) and slowest ($A_3 = 2.5$ m) waves. The space-time surface exhibits a sequence of intersection patterns, with a global maximum of 8.26 m observed during the highest-amplitude collision. Despite this complexity, the three distinct soliton tracks remain identifiable throughout the simulation, consistent with the complete integrability of the KdV equation [4].

Quantitative validation of the soliton dynamics requires comparison of measured propagation velocities against theoretical predictions. Figure 4 presents trajectory data extracted from the spatiotemporal fields using peak detection and tracking algorithms.

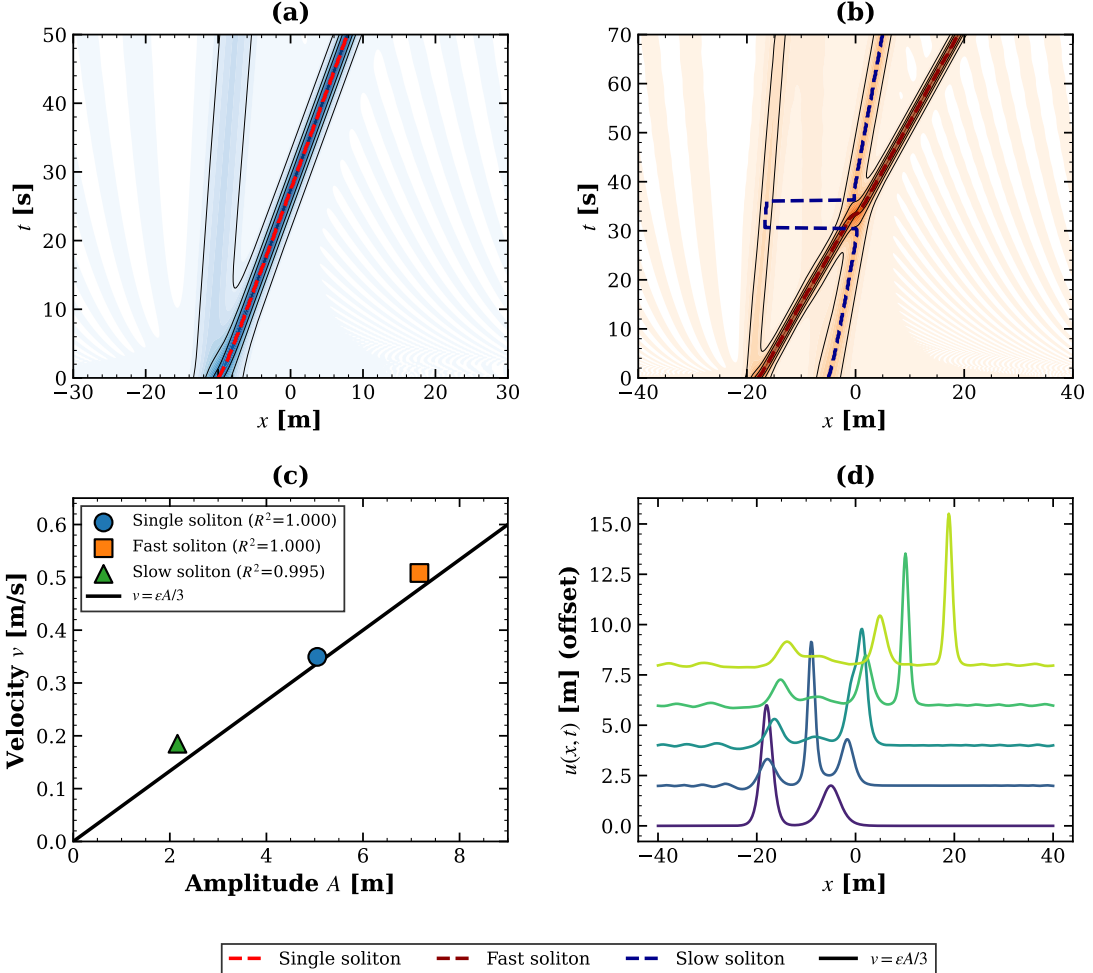


Figure 4: Soliton trajectory analysis. (a) Space-time contour plot for single soliton with tracked trajectory (dashed line); (b) collision case showing fast (dark red) and slow (blue) soliton tracks with collision region indicated; (c) measured velocity versus amplitude with theoretical relation $v = \varepsilon A/3$ (solid line); (d) wave profiles at selected times during collision, vertically offset for clarity.

Panel (a) displays the single-soliton trajectory as a space-time contour plot with the tracked peak position overlaid. The trajectory exhibits excellent linearity, with a coefficient of determination $R^2 = 0.9998$ for the linear fit. The measured amplitude of 5.05 ± 0.29 m (mean \pm standard deviation over the simulation) yields a theoretical velocity of $v_{\text{theo}} = \varepsilon A/3 = 0.337$ m/s according to equation (34). The measured velocity of 0.349 m/s exceeds this prediction by approximately 3.6%, a discrepancy that may be attributed to the amplitude evolution during the initial adjustment phase.

The collision case trajectories, shown in panel (b), reveal the characteristic behavior of an overtaking interaction. The fast soliton ($\text{amplitude } 7.17 \pm 0.39$ m) propagates at a measured velocity of 0.508 m/s with $R^2 = 0.9995$, while the slow soliton ($\text{amplitude } 2.16 \pm 0.10$ m) travels at 0.185 m/s with $R^2 = 0.9950$. The slightly reduced R^2 value for the slow soliton reflects the greater relative perturbation experienced during the collision. The dashed box in panel (b) highlights the collision region where the trajectories temporarily merge before separating.

Panel (c) synthesizes the velocity–amplitude relationship across all tracked solitons. The data points cluster along the theoretical line $v = \varepsilon A/3$, providing quantitative confirmation that the computed solutions satisfy the fundamental KdV dispersion relation. The agreement is particularly notable given that the initial conditions employ approximate sech^2 profiles rather than exact soliton solutions, demonstrating the robustness of the soliton

state as an attractor in the KdV phase space [3].

Panel (d) presents a sequence of wave profiles during the collision event, vertically offset for visualization. The temporal progression illustrates the collision mechanism: the faster soliton approaches from behind, the two waves temporarily merge into a single enhanced peak, and subsequently separate with their original amplitudes restored. This elastic scattering behavior, wherein solitons interact nonlinearly yet emerge unchanged, constitutes the defining characteristic that distinguishes solitons from ordinary wave packets [2].

Beyond trajectory analysis, the spectral structure and information content of the wave field provide complementary diagnostics of solution quality. Figure 5 presents four measures characterizing different aspects of the spatial Fourier decomposition and its evolution.

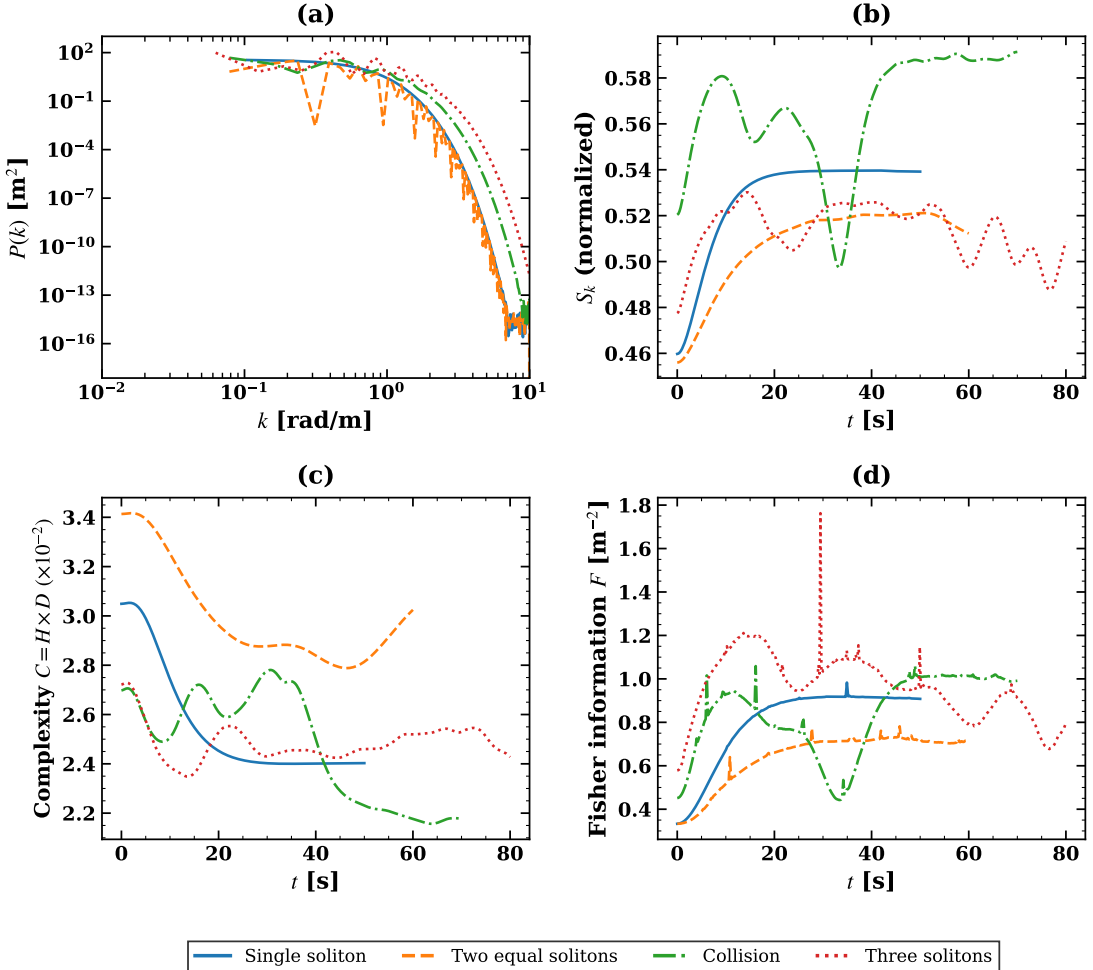


Figure 5: Spectral and information-theoretic analysis. (a) Power spectral density $P(k)$ at initial time for all cases; (b) normalized spectral entropy $S_k(t)$; (c) LMC statistical complexity $C(t) = H \times D$; (d) Fisher information $F(t)$. Line styles as in Figure 2.

Panel (a) displays the initial power spectral density $P(k)$ on logarithmic axes. All cases exhibit similar spectral structure: a plateau at low wavenumbers ($k < 0.1$ rad/m) transitioning to exponential decay at higher wavenumbers, consistent with the smooth sech^2 spatial profiles [18]. The three-soliton case (dotted red) shows the highest total power, reflecting the larger combined amplitude, while the two equal-amplitude case (dashed orange) exhibits oscillatory modulation arising from the spatial interference pattern of the two separated solitons. The spectral decay extends over approximately 15 orders of magnitude before reaching the numerical noise floor near 10^{-16} , confirming that aliasing errors remain negligible for the employed spatial resolutions.

The normalized spectral entropy S_k , plotted in panel (b), quantifies the breadth of the spectral energy distribution according to equation (63). Values near unity indicate uniform spectral content (approaching white noise), while values near zero correspond to energy concentration at a single wavenumber (monochromatic). The soliton solutions exhibit intermediate values in the range 0.46–0.59, reflecting their localized but smooth spatial structure. The single-soliton case shows relatively stable entropy (0.528 ± 0.021), while the collision case displays larger fluctuations (0.567 ± 0.024) with transient increases during the interaction event near $t = 35$ s. These variations suggest temporary spectral broadening as the wave profiles distort during collision, followed by return to the pre-collision distribution as the solitons separate.

The LMC statistical complexity $C = H \times D$, shown in panel (c), provides a measure that distinguishes

structured states from both trivial order and featureless randomness [38]. All cases exhibit complexity values in the range 0.022–0.034, with the two equal-amplitude configuration showing the highest initial complexity ($C_0 = 0.034$) due to the structured interference pattern. The temporal variations appear anticorrelated with spectral entropy: complexity decreases as entropy increases during collision events, consistent with the interpretation that transient spectral broadening reduces the disequilibrium component D while increasing the entropy component H .

Panel (d) presents the Fisher information F , which measures the sharpness or localization of the spatial amplitude distribution according to equation (67). Higher values indicate more localized, sharper-peaked structures. The three-soliton case exhibits the highest mean Fisher information ($0.960 \pm 0.148 \text{ m}^{-2}$), reflecting the presence of multiple narrow peaks, while the two equal-amplitude case shows the lowest ($0.641 \pm 0.119 \text{ m}^{-2}$) due to the broader, lower-amplitude solitons. Notably, the collision case displays pronounced spikes in Fisher information (reaching 1.8 m^{-2}) during the interaction event, reflecting the transient steepening of gradients as the soliton profiles merge. These transient features subsequently relax as the waves separate.

Table 2 summarizes the mean values of the information-theoretic measures across all test cases.

Table 2: Summary of information-theoretic measures (mean \pm standard deviation over simulation time).

| Case | S_k | $C (\times 10^{-2})$ | $F [\text{m}^{-2}]$ |
|--------------------|-------------------|----------------------|---------------------|
| 1 (Single soliton) | 0.528 ± 0.021 | 2.55 ± 0.22 | 0.801 ± 0.180 |
| 2 (Two equal) | 0.508 ± 0.018 | 2.99 ± 0.20 | 0.641 ± 0.119 |
| 3 (Collision) | 0.567 ± 0.024 | 2.47 ± 0.22 | 0.837 ± 0.179 |
| 4 (Three solitons) | 0.514 ± 0.012 | 2.49 ± 0.07 | 0.960 ± 0.148 |

The complete integrability of the KdV equation implies that phase space trajectories are confined to low-dimensional invariant manifolds [5]. RQA provides tools to characterize this structure without requiring explicit identification of action-angle variables. Figure 6 presents phase space diagnostics for the collision case (Case 3) alongside comparison with the single-soliton reference.

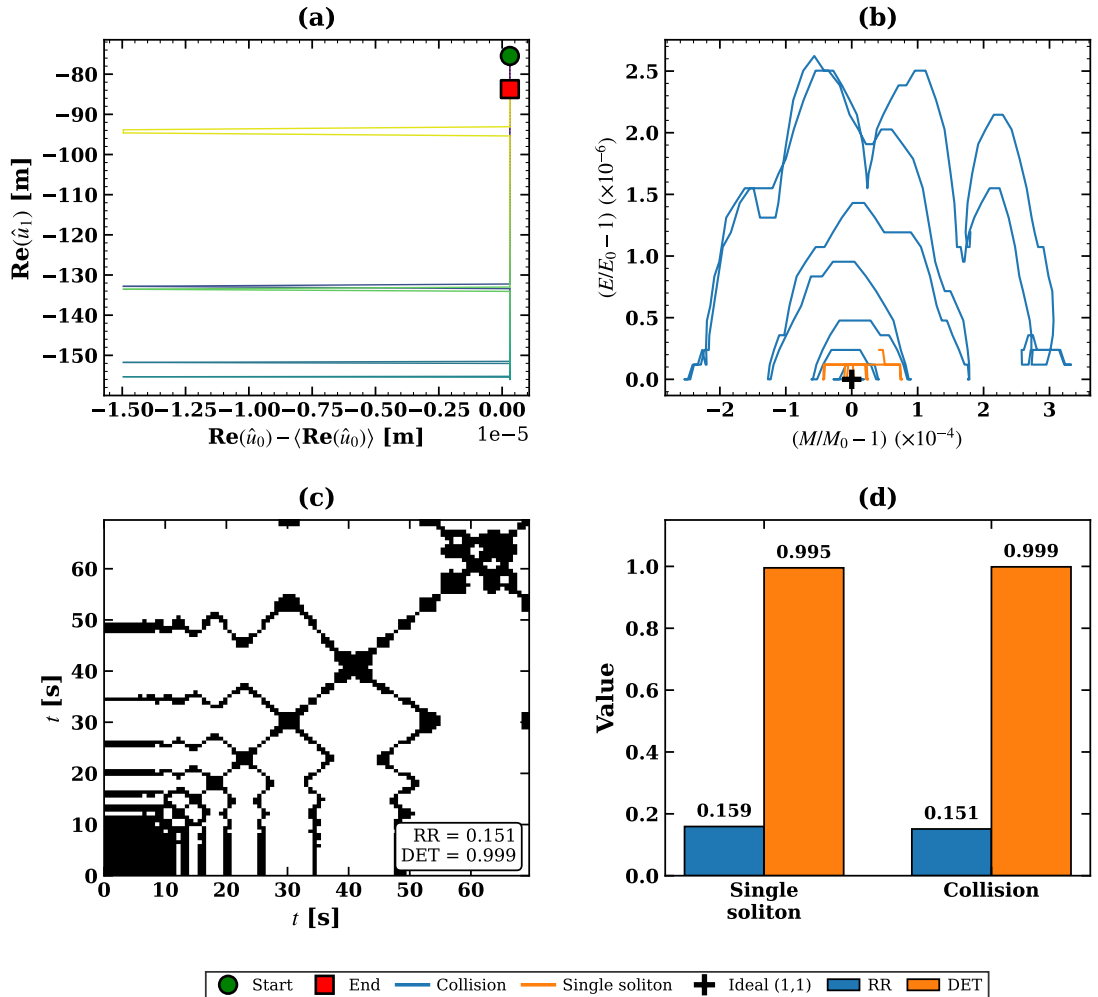


Figure 6: Phase space analysis for the collision case. (a) Trajectory in Fourier mode space (real parts of modes 0 and 1), colored by time; (b) trajectory in normalized conservation space ($M/M_0, E/E_0$); (c) recurrence plot with quantification metrics; (d) comparison of recurrence rate (RR) and determinism (DET) between single-soliton and collision cases.

Panel (a) displays the trajectory in a two-dimensional projection of Fourier mode space, plotting the real part of the first mode $\text{Re}(\hat{u}_1)$ against deviations of the zeroth mode $\text{Re}(\hat{u}_0) - \langle \text{Re}(\hat{u}_0) \rangle$. The zeroth mode, proportional to the spatial mean, exhibited negligible variation ($|\hat{u}_0| = 178.85 \pm 0.00$ m), consistent with mass conservation. Higher modes showed larger fluctuations correlated with collision dynamics: $|\hat{u}_1| = 149.9 \pm 16.0$ m and $|\hat{u}_2| = 97.8 \pm 27.2$ m. The trajectory traces a bounded path in this projection, with the color gradient indicating temporal progression from the start (green circle) to end (red square) of the simulation.

Panel (b) presents the trajectory in normalized conservation space, plotting $(M/M_0 - 1)$ against $(E/E_0 - 1)$. The ideal conservative dynamics would confine the trajectory to a single point at the origin. The computed trajectory remains confined to an extremely small region: $M/M_0 \in [0.9997, 1.0003]$ and $E/E_0 \in [1.0000, 1.0000026]$, with total extent approximately 5.86×10^{-4} . The single-soliton case (orange trace) occupies an even smaller region, while both trajectories cluster near the ideal point (black cross), confirming the high fidelity of the numerical conservation.

The recurrence plot in panel (c) visualizes the binary recurrence matrix R_{ij} defined in equation (71), where black pixels indicate times t_i and t_j at which the conservation space trajectory revisits the same neighborhood (within threshold $\varepsilon = 3.52 \times 10^{-5}$). The diagonal line structures indicate deterministic dynamics: when the system visits a particular state, it subsequently follows a trajectory parallel to previous visits, characteristic of regular (non-chaotic) motion on invariant manifolds [42, 43]. The recurrence rate $\text{RR} = 0.151$ indicates that approximately 15% of state pairs satisfy the recurrence criterion, while the determinism $\text{DET} = 0.999$ confirms that nearly all recurrences form diagonal line structures.

Panel (d) compares the RQA metrics between the single-soliton and collision cases. Both exhibit similar recurrence rates (0.159 and 0.151, respectively) and high determinism (0.995 and 0.999). The marginally higher determinism in the collision case may appear counterintuitive but likely reflects the longer simulation time (70 s versus 50 s) providing more opportunities for trajectory segments to align. A correlation dimension estimate of 0.86 for the collision case, computed from the recurrence matrix scaling [43], suggests that the effective dynamics occupy a manifold of dimension less than unity—consistent with the trajectory being confined near a fixed point

(the ideal conservation state) with small bounded oscillations.

The results presented above demonstrate that the `sangkuriang` solver successfully reproduces the essential features of KdV soliton dynamics while maintaining numerical accuracy appropriate for research applications. Several aspects merit further discussion.

The pseudo-spectral spatial discretization combined with eighth-order adaptive time integration achieved conservation errors ranging from $\mathcal{O}(10^{-7})$ to $\mathcal{O}(10^{-4})$ across the test cases. These values compare favorably with those reported in the literature for similar methods applied to nonlinear dispersive equations [17, 20]. The observation that momentum and energy are conserved more accurately than mass warrants consideration. The mass functional (30) involves only the solution field itself, making it sensitive to any drift in the solution mean. In contrast, the momentum functional (31) depends on u^2 , which suppresses the contribution of small-amplitude dispersive radiation relative to the dominant soliton peaks. The energy functional (32), involving spatial derivatives, further weights the smooth soliton cores over high-wavenumber numerical artifacts. This hierarchy suggests that the mass error may serve as a conservative upper bound on overall numerical accuracy.

The absence of systematic drift in the conservation time series indicates that the DOP853 integrator, while not symplectic, introduces primarily oscillatory rather than secular errors for the integration times considered. For significantly longer simulations, the accumulation of these oscillatory errors could potentially become problematic, and structure-preserving integrators [36, 44] might offer advantages despite their typically higher computational cost per step.

The close agreement between measured and theoretical soliton velocities ($< 5\%$ discrepancy) confirms that the computed solutions satisfy the fundamental amplitude–velocity relationship (34). The small systematic excess in measured velocities relative to predictions based on mean amplitude may arise from several factors. First, the soliton amplitudes evolve during the initial adjustment phase as the approximate initial conditions relax toward exact soliton profiles, and velocity measurements based on trajectory slopes integrate over this transient. Second, the theoretical velocity assumes an isolated soliton in an infinite domain, whereas the periodic boundary conditions and finite domain introduce corrections that may slightly modify the effective dispersion relation [18].

The high linearity of all tracked trajectories ($R^2 > 0.99$) provides strong evidence that the computed waves behave as true solitons rather than dispersive wave packets that would spread and decelerate over time. This validation is particularly meaningful for the post-collision segments, where any deviation from integrability would manifest as amplitude-dependent velocity changes.

The spectral and information-theoretic analyses reveal consistent patterns that reflect the integrable structure of the KdV equation. The bounded variations of spectral entropy, statistical complexity, and Fisher information—with transient excursions during collisions that subsequently relax—indicate that the wave field returns to its pre-collision information content. This behavior contrasts with what would be expected for non-integrable systems, where collision events could transfer energy to radiation modes, leading to secular changes in these measures [6].

The Fisher information proved particularly sensitive to collision dynamics, with pronounced spikes corresponding to the transient steepening of gradients during wave merging. This sensitivity suggests that Fisher information may serve as a useful diagnostic for detecting the onset and completion of soliton interactions in more complex scenarios.

The RQA provides independent confirmation of the regular, non-chaotic dynamics expected for an integrable Hamiltonian system. The high determinism values ($\text{DET} > 0.99$) indicate that the phase space trajectory exhibits the parallel structure characteristic of motion on invariant tori, rather than the mixing behavior associated with chaotic dynamics [43]. The estimated correlation dimension below unity is consistent with the trajectory being confined near a fixed point (the exact conservation state) with small-amplitude oscillations.

These results suggest that RQA could serve as a model-independent diagnostic for assessing the integrability of computed solutions in situations where analytical results are unavailable. Significant deviations from high determinism might indicate either numerical breakdown of integrability due to insufficient resolution, or genuine non-integrable dynamics in perturbed KdV-type equations.

The demonstration that research-grade KdV simulations can be performed in minutes on a laptop-class workstation represents a practical advantage for exploratory studies. The Numba-accelerated implementation achieved throughputs of approximately 1000–1400 time steps per second, suggesting that the solver is not severely memory-bandwidth limited for the grid sizes considered. The observed scaling from $N = 512$ to $N = 1024$ (throughput reduction from ~ 1300 to ~ 1030 steps/s) is consistent with the $\mathcal{O}(N \log N)$ FFT complexity combined with increased cache pressure.

For applications requiring higher resolution or longer integration times, several optimization strategies could be considered: vectorized evaluation of multiple initial conditions in parallel, GPU acceleration of FFT operations via CuPy [45], or time-parallel algorithms for ensemble simulations. The modular architecture of `sangkuriang` is designed to facilitate such extensions while maintaining compatibility with the existing analysis framework.

Several limitations of the present study should be acknowledged. First, the test cases employed approximate sech^2 initial conditions rather than exact N -soliton solutions obtainable from inverse scattering theory [5]; comparison with exact solutions would provide a more stringent validation. Second, the periodic boundary conditions preclude investigation of soliton interactions with boundaries or non-periodic wave backgrounds. Third, the standard KdV equation considered here represents only the leading-order balance between nonlinearity and dispersion; extensions to higher-order equations (e.g., the modified KdV or Kawahara equations [46]) would broaden the solver’s applicability to different physical regimes.

Future development of `sangkuriang` could address these limitations while maintaining the design philosophy of accessibility and reproducibility. The integration of inverse scattering routines would enable exact initial conditions for validation studies. Variable-coefficient extensions would permit modeling of wave propagation over varying topography. Perhaps most significantly, the pseudo-spectral framework could be extended to two-dimensional generalizations such as the Kadomtsev–Petviashvili equation [6], enabling investigation of oblique soliton interactions and transverse instabilities.

4 Conclusions

This work has presented `sangkuriang`, an open-source pseudo-spectral solver for the KdV equation that combines Fourier-based spatial discretization with adaptive eighth-order time integration. Validation across four test cases—ranging from isolated soliton propagation to three-body interactions—demonstrated conservation of the KdV invariants to relative errors below 10^{-5} for momentum and energy, while measured soliton velocities agreed with theoretical predictions to within 5%. The information-theoretic diagnostics revealed bounded spectral entropy and high phase-space determinism throughout all simulations, consistent with the integrable structure of the governing equation. Implemented in Python with Numba acceleration, the solver achieved practical throughput on modest hardware, completing the most demanding test case in under ten minutes on a laptop workstation. The combination of numerical accuracy, physical fidelity, and computational accessibility suggests that `sangkuriang` may serve as a useful tool for both pedagogical exploration of nonlinear wave phenomena and preliminary research investigations of soliton dynamics in dispersive media.

Acknowledgments

S.H.S.H. was supported by the Dean’s Distinguished Fellowship 2023 from the University of California, Riverside. F.K., I.P.A., and D.E.I. were supported by the Research, Community Service and Innovation Program (FITB.PPMI-1-04-2025) and Early Career Research Scheme through the Directorate of Research and Innovation (2352/IT1.B07.1/TA.00/2025) from Bandung Institute of Technology.

Author Contributions

S.H.S.H.: Conceptualization; Formal analysis; Investigation; Methodology; Software; Validation; Visualization; Funding acquisition; Writing – original draft; Project administration. F.K.: Methodology; Funding acquisition; Writing – review & editing. I.P.A.: Funding acquisition; Supervision; Writing – review & editing. D.E.I.: Funding acquisition; Supervision; Writing – review & editing. All authors reviewed and approved the final version of the manuscript.

Open Research

The `sangkuriang` library source code is available on GitHub at <https://github.com/sandyherho/sangkuriang-ideal-solver> under the WTFPL license and can be installed from PyPI at <https://pypi.org/project/sangkuriang-ideal-solver/>. The Python scripts for data analysis (https://github.com/sandyherho/suppl_sangkuriang) and all simulation outputs—including animations, NetCDF data files, figures, computational logs, and statistical analyses—archived on the Open Science Framework (OSF) (<https://doi.org/10.17605/OSF.IO/MS5EJ>) are released under the MIT license.

References

- [1] D. J. Korteweg and G. de Vries, “On the change of form of long waves advancing in a rectangular canal, and on a new type of long stationary waves,” *Philos. Mag.* **39**, 422 (1895). <https://doi.org/10.1080/14786449508620739>
- [2] N. J. Zabusky and M. D. Kruskal, “Interaction of ‘solitons’ in a collisionless plasma and the recurrence of initial states,” *Phys. Rev. Lett.* **15**, 240 (1965). <https://doi.org/10.1103/PhysRevLett.15.240>
- [3] P. G. Drazin and R. S. Johnson, *Solitons: An Introduction*, 2nd ed. (Cambridge University Press, Cambridge, 1989). <https://doi.org/10.1017/CBO9781139172059>
- [4] C. S. Gardner, J. M. Greene, M. D. Kruskal, and R. M. Miura, “Method for solving the Korteweg-deVries equation,” *Phys. Rev. Lett.* **19**, 1095 (1967). <https://doi.org/10.1103/PhysRevLett.19.1095>
- [5] M. J. Ablowitz, D. J. Kaup, A. C. Newell, and H. Segur, “The inverse scattering transform-Fourier analysis for nonlinear problems,” *Stud. Appl. Math.* **53**, 249 (1974). <https://doi.org/10.1002/sapm1974534249>
- [6] M. J. Ablowitz, *Nonlinear Dispersive Waves: Asymptotic Analysis and Solitons* (Cambridge University Press, Cambridge, 2012). <https://doi.org/10.1017/CBO9780511998324>
- [7] G. B. Whitham, *Linear and Nonlinear Waves* (John Wiley & Sons, New York, 1999). <https://doi.org/10.1002/9781118032954>
- [8] D. R. Durran, *Numerical Methods for Fluid Dynamics: With Applications to Geophysics* (Springer, New York, 2010). <https://doi.org/10.1007/978-1-4419-6412-0>
- [9] S. H. S. Herho, F. R. Fajary, K. E. P. Herho, I. P. Anwar, R. Suwarman, and D. E. Irawan, “Reappraising double pendulum dynamics across multiple computational platforms,” *CLEI Electron. J.* **28**, 10 (2025).

<https://doi.org/10.19153/cleiej.28.1.10>

[10] S. H. S. Herho, S. N. Kaban, and C. Nugraha, “OptionMC: A Python package for Monte Carlo pricing of European options,” *Int. J. Data Sci.* **6**, 70 (2025). <https://doi.org/10.18517/ijods.6.2.70-84.2025>

[11] C. R. Harris *et al.*, “Array programming with NumPy,” *Nature* **585**, 357 (2020). <https://doi.org/10.1038/s41586-020-2649-2>

[12] P. Virtanen *et al.*, “SciPy 1.0: Fundamental algorithms for scientific computing in Python,” *Nat. Methods* **17**, 261 (2020). <https://doi.org/10.1038/s41592-019-0686-2>

[13] S. K. Lam, A. Pitrou, and S. Seibert, “Numba: A LLVM-based Python JIT compiler,” in *Proceedings of the Second Workshop on the LLVM Compiler Infrastructure in HPC* (ACM, New York, 2015), pp. 1–6. <https://doi.org/10.1145/2833157.2833162>

[14] S. H. S. Herho *et al.*, “kh2d-solver: A Python library for idealized two-dimensional incompressible Kelvin-Helmholtz instability,” *Appl. Comput. Mech.* **19**, 125 (2025). <https://doi.org/10.24132/acm.2025.1040>

[15] M. P. Pavlenko, L. V. Pavlenko, Y. V. Iotov, and Y. M. Pavlenko, “Experience in the development and implementation of the course ‘Python for Physics Teachers’,” *J. Phys. Conf. Ser.* **3105**, 012011 (2025). <https://doi.org/10.1088/1742-6596/3105/1/012011>

[16] E. Tufino, S. Oss, and M. Alemani, “Integrating Python data analysis in an existing introductory laboratory course,” *Eur. J. Phys.* **45**, 045707 (2024). <https://doi.org/10.1088/1361-6404/ad4fcc>

[17] L. N. Trefethen, *Spectral Methods in MATLAB* (SIAM, Philadelphia, 2000). <https://doi.org/10.1137/1.9780898719598>

[18] J. P. Boyd, *Chebyshev and Fourier Spectral Methods*, 2nd ed. (Dover Publications, Mineola, NY, 2001).

[19] C. Canuto, M. Y. Hussaini, A. Quarteroni, and T. A. Zang, *Spectral Methods: Evolution to Complex Geometries and Applications to Fluid Dynamics* (Springer, Berlin, 2007). <https://doi.org/10.1007/978-3-540-30728-0>

[20] B. Fornberg, *A Practical Guide to Pseudospectral Methods* (Cambridge University Press, Cambridge, 2009). <https://doi.org/10.1017/CBO9780511626357>

[21] J. R. Dormand and P. J. Prince, “A family of embedded Runge-Kutta formulae,” *J. Comput. Appl. Math.* **6**, 19 (1980). [https://doi.org/10.1016/0771-050X\(80\)90013-3](https://doi.org/10.1016/0771-050X(80)90013-3)

[22] E. Hairer, G. Wanner, and S. P. Nørsett, *Solving Ordinary Differential Equations I: Nonstiff Problems*, 2nd ed. (Springer, Berlin, 1993). <https://doi.org/10.1007/978-3-540-78862-1>

[23] R. Rew and G. Davis, “NetCDF: An interface for scientific data access,” *IEEE Comput. Graph. Appl.* **10**, 76 (1990). <https://doi.org/10.1109/38.56302>

[24] M. W. Dingemans, *Water Wave Propagation Over Uneven Bottoms: Part 1* (World Scientific, Singapore, 1997). <https://doi.org/10.1142/1241-part1>

[25] M. W. Dingemans, *Water Wave Propagation Over Uneven Bottoms: Part 2* (World Scientific, Singapore, 1997). <https://doi.org/10.1142/1241-part2>

[26] R. S. Johnson, *A Modern Introduction to the Mathematical Theory of Water Waves* (Cambridge University Press, Cambridge, 1997). <https://doi.org/10.1017/CBO9780511624056>

[27] C. C. Mei, *The Applied Dynamics of Ocean Surface Waves* (World Scientific, Singapore, 1992). <https://doi.org/10.1142/0752>

[28] R. M. Miura, “Korteweg-de Vries equation and generalizations. I. A remarkable explicit nonlinear transformation,” *J. Math. Phys.* **9**, 1202 (1968). <https://doi.org/10.1063/1.1664700>

[29] E. O. Brigham, *The Fast Fourier Transform and Its Applications* (Prentice-Hall, Upper Saddle River, NJ, 1988).

[30] J. W. Cooley and J. W. Tukey, “An algorithm for the machine calculation of complex Fourier series,” *Math. Comput.* **19**, 297 (1965). <https://doi.org/10.1090/S0025-5718-1965-0178586-1>

[31] D. Gottlieb and S. A. Orszag, *Numerical Analysis of Spectral Methods: Theory and Applications* (SIAM, Philadelphia, 1977). <https://doi.org/10.1137/1.9781611970425>

[32] P. J. Prince and J. R. Dormand, “High order embedded Runge-Kutta formulae,” *J. Comput. Appl. Math.* **7**, 67 (1981). [https://doi.org/10.1016/0771-050X\(81\)90010-3](https://doi.org/10.1016/0771-050X(81)90010-3)

[33] T. J. Bridges and S. Reich, “Numerical methods for Hamiltonian PDEs,” *J. Phys. A: Math. Gen.* **39**, 5287 (2006). <https://doi.org/10.1088/0305-4470/39/19/S02>

[34] K. E. Atkinson, *An Introduction to Numerical Analysis*, 2nd ed. (John Wiley & Sons, New York, 1991).

[35] J. D. Hunter, “Matplotlib: A 2D graphics environment,” *Comput. Sci. Eng.* **9**, 90 (2007). <https://doi.org/10.1109/MCSE.2007.55>

[36] T. J. Bridges and S. Reich, “Numerical methods for Hamiltonian PDEs,” *J. Phys. A: Math. Gen.* **39**, 5287 (2006). <https://doi.org/10.1088/0305-4470/39/19/S02>

[37] C. E. Shannon, “A mathematical theory of communication,” *Bell Syst. Tech. J.* **27**, 379 (1948). <https://doi.org/10.1002/j.1538-7305.1948.tb01338.x>

[38] R. López-Ruiz, H. L. Mancini, and X. Calbet, “A statistical measure of complexity,” *Phys. Lett. A* **209**, 321 (1995). [https://doi.org/10.1016/0375-9601\(95\)00867-5](https://doi.org/10.1016/0375-9601(95)00867-5)

[39] R. A. Fisher, “Theory of statistical estimation,” *Math. Proc. Cambridge Philos. Soc.* **22**, 700 (1925). <https://doi.org/10.1017/S0305004100009580>

[40] B. R. Frieden, *Science from Fisher Information: A Unification* (Cambridge University Press, Cambridge, 2004). <https://doi.org/10.1017/CBO9780511616907>

- [41] A. Ly, M. Marsman, J. Verhagen, R. P. P. P. Grasman, and E.-J. Wagenmakers, “A tutorial on Fisher information,” *J. Math. Psychol.* **80**, 40 (2017). <https://doi.org/10.1016/j.jmp.2017.05.006>
- [42] J.-P. Eckmann, S. O. Kamphorst, and D. Ruelle, “Recurrence plots of dynamical systems,” *Europhys. Lett.* **4**, 973 (1987). <https://doi.org/10.1209/0295-5075/4/9/004>
- [43] N. Marwan, M. C. Romano, M. Thiel, and J. Kurths, “Recurrence plots for the analysis of complex systems,” *Phys. Rep.* **438**, 237 (2007). <https://doi.org/10.1016/j.physrep.2006.11.001>
- [44] E. Hairer, G. Wanner, and C. Lubich, *Geometric Numerical Integration: Structure-Preserving Algorithms for Ordinary Differential Equations*, 2nd ed. (Springer, Berlin, 2006). <https://doi.org/10.1007/3-540-30666-8>
- [45] R. Okuta, Y. Unno, D. Nishino, S. Hido, and C. Loomis, “CuPy: A NumPy-compatible library for NVIDIA GPU calculations,” in *Proceedings of the Workshop on Machine Learning Systems, NIPS* (2017). http://learningsys.org/nips17/assets/papers/paper_16.pdf
- [46] T. Kawahara, “Oscillatory solitary waves in dispersive media,” *J. Phys. Soc. Jpn.* **33**, 260 (1972). <https://doi.org/10.1143/JPSJ.33.260>